Article:

Curry, R.J. and Langdon, G.S. orcid.org/0000-0002-0396-9787 (2021) The effect of explosive charge backing in close-proximity air-blast loading. International Journal of Impact Engineering, 151. 103822. ISSN 0734-743X

https://doi.org/10.1016/j.ijimpeng.2021.103822

The effect of explosive charge backing in close-proximity air-blast loading

R.J. Curry[1,2]*, G.S. Langdon[1,2]

[1]Blast Impact and Survivability Research Unit, Department of Mechanical Engineering, University of Cape Town, Rondebosch, 7700, South Africa.

[2]Department of Civil and Structural Engineering, University of Sheffield, Sheffield, S13JD, UK.

Email: r.curry@sheffield.ac.uk

Abstract

This paper presents new insights into the influence of explosive charge backing on the impulse transfer and transient response characteristics of plates subjected to close-proximity air blast loading. The results of the combine experimental and computational studies show the critical influence of charge backing, which caused between a 3-5 times increase in the impulse transfer when the charge was metal-backed. The permanent deflections from the metal-backed detonations were larger than for air, but not to the same degree as the impulse increase. These findings demonstrate the important influence of charge backing, in close proximity detonations, which greatly exceeded anything previously measured. These valuable insights will assist blast protection engineers considering the effects of explosions in situations when the charge backing is something other than air, which is a frequent occurrence in explosion scenarios.

Keywords: blast response, plates, plastic deformation, transient response, charge backing

1. Introduction

After more than a decade of increased awareness of subversive activity, the public expects protection from the threat of explosions. Explosive threats can be accidental such as the recent blast in a Chinese industrial park that killed 19 people (1) and the tragic death of an American caused by an "exploding electronic cigarette" (2). Unfortunately, deliberate explosions, such as terrorist activity, landmine detonations or military action are far too common. A great deal of effort has gone into preventing deliberate explosive detonations, such as better pre-screening at airports and active mitigation methods in military systems. Despite this, terrorist attacks still caused the deaths of at least 25,673 people in 2016 (3), with explosions accounting for 54% of the attacks. Anti-vehicle landmines were involved in 169 incidents in 2017, injuring 321 people and killing 166 people (4).

Landmines are typically disc-shaped and have a diameter (D) to height (H) ratio of approximately three. Most anti-vehicle landmines are buried or laid on the ground. This means that the detonated explosives have a backing that influences the blast wave development. There are also accounts of horizontally-mounted mines targeting vulnerable parts of passing vehicles (5). Anti-personnel landmines are smaller the anti-vehicle mines but cause more deaths because of their ubiquitous use. The Landmine Monitor Report (5) recorded over 122,000 casualties from anti-personnel landmines and explosive remnants of war (including 36,000 deaths) over a twenty-year period (6).

Bare, disk-shaped (that is, high D/H ratio cylindrical), charges generate complex blast waves that propagate away from the detonation location. The influence of charge shape decreases in importance as stand-off distance (SOD) increases (7). The Hopkinson–Cranz scaled distance, $Z = R/W^{1/3}$ (where R is the SOD from the charge to the target and W is the TNT equivalent charge mass) is a dimensional scaled distance. Explosions are considered ‘near-field’ for $Z < 1$ m/kg$^{1/3}$, and in this region the blast pressure and impulse distribution is extremely non-uniform and fireball effects are significant (8) (9) (10). Spherical blast waves propagate in the axial and radial directions after the detonation of a cylindrical charge (9) (8). Bridge waves can form following detonations in free air, reinforced by interactions between the axial and radial wave propagation (6).

Xiao et al (11) modelled the detonation of cylindrical TNT charges in free air with D/H values ranging from 0.2 to 1 (which is too low for landmine detonations). When $Z = 0.7$ m/kg$^{1/3}$, the shock wave was highly focused in the axial direction when the cylinders were detonated at a single end, rather than centre-detonated. Charge shape effects had insignificant effect on pressure when $Z > 3.9$ m/kg$^{1/3}$ and impulse effects could be neglected when $Z > 5.7$ m/kg$^{1/3}$. Qi et al (12) performed experimental and computational studies into the influence of charge shape on the axial impulse generated and flight characteristics of a ball bearing during end-detonations of PE4 cylinders. The overall axial impulse increased but the ball bearing velocity decreased as D/H increased (for a constant charge mass).

Although surface bursts are frequent in practice, most studies consider free air detonations (for example, references (6) (7) (9) (8), (11) (12)) while relatively few focus on surface bursts (13) (14) (15) (16). Guerke and Scheklinski-Gluek (13) performed tests on cylinders of RDX (D/H=0.2 and D/H=1) inclined at different angles to the ground for 0.5 m/kg$^{1/3} < Z < 32$ m/kg$^{1/3}$. Preliminary results attributed the variations between the cylindrical and hemispherical tests to differences in the time and shape of the detonation waves reaching the air. The pressure propagation over distance (in the far-field) was observed to be a combination of the shock front differences, the interaction between axial and radial blast waves and multiple pressure reflections. Tancreto (14) investigated the effect of charge shape on the impulse and overpressure generated from surface bursts involving the detonation of hemispherical and cylindrical Composition B charges. Charge shape effects were significant, increasing both the overpressure and impulse for $Z < 8$ m/kg$^{1/3}$.

Xiao et al (15) performed similar work to the free air simulations reported in reference (11), comparing hemispherical charge and cylindrical charge detonations on the ground. The model results were validated using the data presented by Tancreto (14). The influence of the charge shape was found to be significant for overpressures up to $Z = 4$ m/kg$^{1/3}$, while the impulse effect persisted until $Z = 8.0$ m/kg$^{1/3}$ when the cylindrical charge was end detonated. The impulse predictions were 20% higher in the far-field for cylindrical detonations (compared to hemispherical ones).

Explosions in, or on, the ground transmit energy to their surroundings. This energy release takes many forms, including heat, air and soil kinetic energy, soil deformation and work done by expanding gaseous products. Several factors affect the energy partition. For example, when an explosion occurs far under the surface of the ground, the energy is totally absorbed by soil deformation, mechanical losses and thermal losses (16). At the other extreme is a surface detonation on frozen soil, where very little energy is transmitted to the ground and the air shock and impingement of the detonation products do much of the work on nearby structures. Many factors influence the total impulse transfer to a structure, including moisture content and bulk density of the soil (17) (18) (19) (20) (21), the size of the granular particles (20), the SOD (17), (20) (22) (23) and the depth of burial (DOB) (17), (20) (22) (23).

Recently, Clarke et al (24) presented results from a detailed parametric study, comprising 40 tests at quarter scale, into the effect of charge placement, soil composition, moisture content and geometrical confinement on the loading that arose from explosive detonations in soil. Part of the study compared D/H=3, disk-shaped, 78g PE4 charge detonations with only air behind the charge to results from soil backed surface detonations with the same charge geometry ($Z < 0.37$ m/kg$^{1/3}$). The pressure was slightly more localised and exhibited a higher peak value when the charge was soil-backed. There were no discernible differences in the total impulse, specific impulse or time to peak pressure.

Commercial landmine protected vehicle testing allows for the use of controlled simulated charges, as outlined in NATO Stanag 4569 AEP-55 Vol 2 (25). This provides a reference guide for the standardised testing of vehicles subjected to simulated mine detonation. One of the standard test methods involves mounting a charge on a metal backing plate, as shown in Figure 1. The target is a reference plate, with a span to thickness ratio of between 33 and 50, manufactured from steel plate. Voisin *et al* (26) used the arrangement shown in Figure 1 to compare the response of composite panels to simulated landmine loading, but do not consider the influence of the backing plate on the loading or structural response.

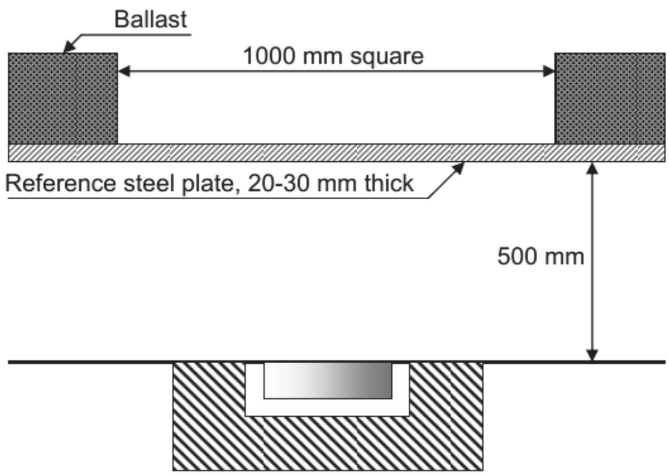

Figure 1 A Proposed configuration for simulated mine detonation tests (25)

Extensive experimental studies have reported on the large permanent ductile deformation and rupture of plates, beams and shells due to blast loading conditions in air. Jones (27), Nurick and Martin (28; 29), and Chung Kim Yuen et al (30) present overviews of theoretical and experimental studies of plates subjected to impulsive and/or air-blast loading. Comparable information concerning the influence of a solid backing to an explosive charge on the impulse imparted to a structure and the damage that ensues is not available.

This paper reports the results of experimental and computational studies on the influence of charge backing on the impulse transfer and deformation characteristics of steel plates subjected to air-blast loading. The paper provides detailed insights that are of great practical relevance to blast protection engineers considering explosions on the ground or other solid backings, such as landmine protection research. The paper is arranged as follows. The experimental arrangements and test results are described in sections 2 and 3 respectively. Results from blast tests on fully-clamped Domex steel plates are reported, including the transient response obtained from high speed images recorded during the blast experiments. Section 4 describes the computational modelling approach, involving LS-Dyna simulations of the experiments. The simulation results are used, alongside the experiments, to provide important insights into the influence of charge mass and charge backing type (either air or steel) on the impulse transfer, transient response and permanent deformation of steel plates.

2. Experimental Method

2.1 Test Specimens

Following Curry and Langdon (31), square test plates, with a side length of 400 mm, were manufactured from 3mm thick Domex 355MC, a high strength hot-rolled low alloy steel. Results from quasi-static tensile tests found the following material properties: mean average yield strength was 444 MPa, ultimate tensile strength was 627 MPa and the percentage elongation at failure was 20%. Further details on the material characterisation are available in references (32) (31). For blast testing, the 400 mm by 400 mm square plates were mounted between two picture frame clamps as shown in Figure 2. When placed in the clamp frame, the plates had a circular exposed area with a diameter of 300 mm.

2.2 Air-blast loading

Each test plate was cleaned and painted with a speckle pattern for filming purposes. The plates were bolted into a chamfered clamp frame, as shown in Figure 2. A 38 mm diameter cylinder was moulded from Plastic Explosive #4 (PE4) for each experiment. The diameter was kept constant while the charge height was varied depending on the charge mass. The SOD was measured from the face of the charge. Two SODs, 40 mm and 50 mm, and two charge backing configurations were used: (1) air backed charges, and (2) steel-backed charges. The two configurations are shown in the schematics in Figure 3. The steel backing comprised a 20 mm thick steel plate (400 wide and 400 mm long) on a compressed sand foundation. Each charge was detonated at the centre of the rear face of the charge using an electrical detonator. For the metal-backed charges, the detonator was pushed through a small hole in the centre of the steel backing plate. The backing plate was inspected after each test and replaced if damaged.

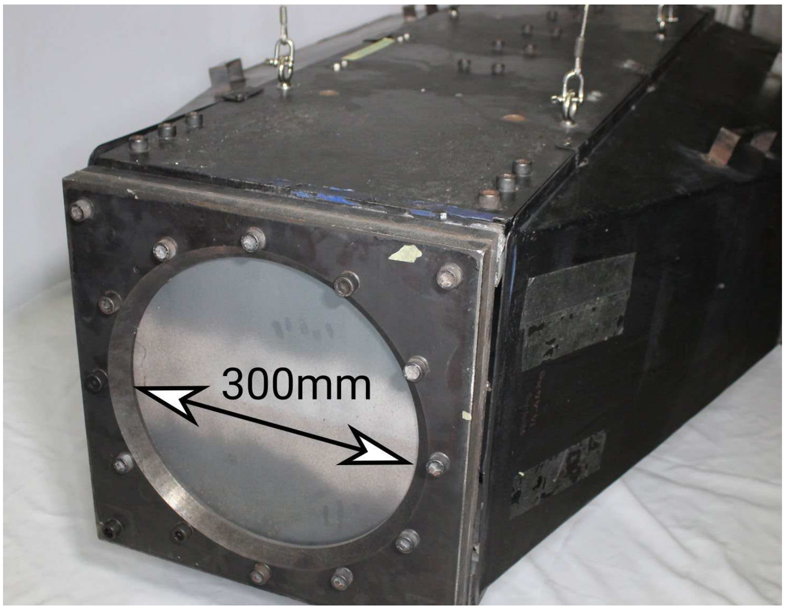

Figure 2 Photograph of a steel test plate and clamp frame on the horizontal pendulum (32)

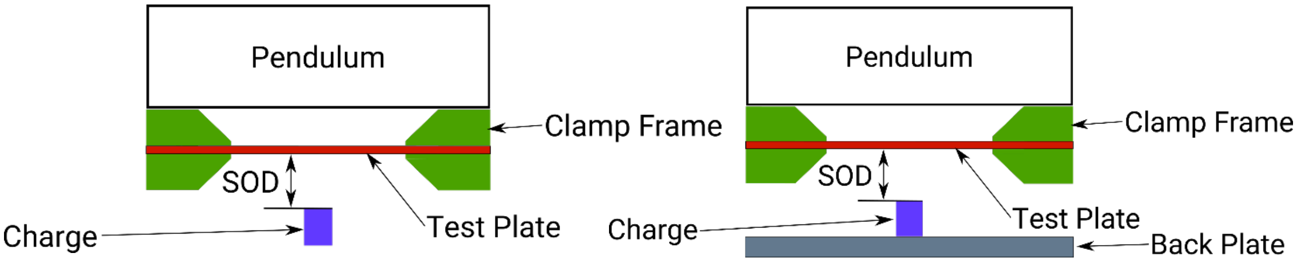

Figure 3: Schematics showing the test configurations (a) air-backed charges, (b) metal-backed charges

2.3 Instrumentation

Two high-speed monochrome IDT NRS4 cameras, filming at 30 000 fps, were used to record the rear plate surface during the blast experiments. The cameras were triggered with a custom built TTL trigger circuit that was activated by the detonation of the charge and an electrical synchronous trigger was employed. The cameras were mounted on a rail system to isolate them from vibration, as shown in Figure 4. Each camera was focused on the central strip through the middle of the test plate, resulting in data reflecting the transient displacement on the central midpoint as well as the cross section of the whole plate. Additional LED lights, covered by a diffuser, provided sufficient lighting to achieve good images for a 31 µs exposure time. The impulse transferred to the plates was calculated using the maximum swing of the pendulum and a simple single-degree-of-freedom analysis. Metal shrouding was used around the pendulum to isolate the cameras from the intense light emissions and shock loading arising from the detonation of plastic explosives. Following the experiments, the plates were scanned using a 3D scanner to obtain surface plots of the deformed rear surface.

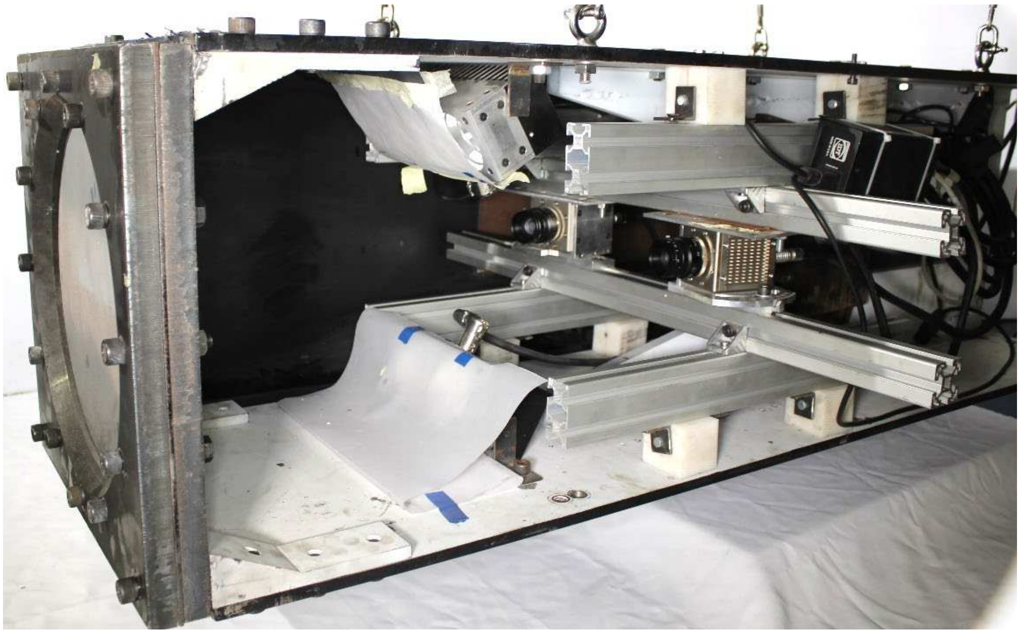

Figure 4: Photograph showing the high-speed imaging system mounted to the pendulum (shrouding removed for clarity) (38)

The camera images were post-processed using the Dantec Dynamics Istra 4D DIC software package. Prior to testing, calibration was performed to find the intrinsic and extrinsic imaging parameters). Multiple images of the calibration target (which had a known checkerboard pattern) were captured at different positions (using both cameras). The software then processed these images and calculated the projection parameter of the entire system and additional distortion parameters, using the pinhole model. The intrinsic and extrinsic calibration values for the system were stored in a calibration file and imported into the analysis. Typically, eight images were sufficient to calculate all calibration parameters accurately.

During post-processing, the specimen deformation was determined by tracking the movement of the speckle pattern using a correlation algorithm to minimise the errors. For this set of tests, an equivalence of 1 pixel = 0.3 mm meant that the worst uncertainty in the DIC data would give an equivalent error of less than 1.5 mm in the deformation data. Subset sizes were fixed at 19 pixels with a grid spacing of 5 pixels to ensure overlap in the subsets. Once a displacement field was calculated for the area of interest, other information such as the strain field could be calculated. All data presented in this paper are the unfiltered results exported from the DIC software. Data was extracted along a centre line indicated on the plate using two markers, and mid-point displacement was calculated. The data was post processed using a custom python script to align and plot the displacement information for each line, and to align the profiles with the 3D scans of the plates. Further details regarding the DIC calibration, analysis and post-processing are available in references (32) (31).

3. Blast test results

The results from metal-backed charge detonation experiments are summarised in Table 1. The air-backed detonation test results are taken from Curry and Langdon (31) and are not repeated in the table. All the plates, regardless of charge backing type, exhibited Mode 1 (that is, large plastic deformation) failure without any indication of tearing or shearing failures.

Table 1: Summary of metal-backed detonation test results

SOD (mm)	Test designation	Charge Mass (g)	Impulse (Ns)	δPerm (mm)	δPeak (mm)
40	M25-40-01	25	126,9	38,4	42,7
	M20-40-01	20	131,7	35,6	40,8
	M20-40-02	20	118,9	33,3	
	M15-40-01	15	111,7	29,6	
	M15-40-02	15	106,2	28,0	
	M15-40-03	15	115,6	31,8	
	M15-40-04	15	110,2	31,5	37,2
	M15-40-05	15	117,2	28,2	33,4
	M10-40-01	10	92,2	21,9	
	M10-40-02	10	95,0	21,7	
	M10-40-03	10	93,1	26.0	31,8
50	M25-50-01	25	120,2	34,4	36,3
	M20-50-01	20	110,6	30.0	37,1
	M20-50-02	20	117,2	29,7	
	M20-50-03	20	106,7	26,0	
	M15-50-01	15	106,3	23,7	
	M15-50-02	15	104.0	23,6	
	M15-50-03	15	90,7	24,3	29,8
	M10-50-01	10	88,0	21,9	28,3
	M10-50-02	10	89,0	22,3	28,2
	M10-50-03	10	80,0	20,6	
	M10-50-04	10	88,0	21,2	

3.1 Impulse transfer characteristics

Figure 5 shows graphs of impulse versus charge mass for the air and metal-back charge detonations at 40 and 50 mm SOD. As expected, there is a linear relationship between impulse and charge mass for each load condition. For a given SOD, the metal backing caused an increase in the impulse measured on the pendulum. Both the gradient and the intercept of the linear trend-lines increased when a metal-backing was introduced: the slope doubled and the intercept increased by 67 Ns for the 40 mm SOD and 57 Ns for the 50 mm SOD.

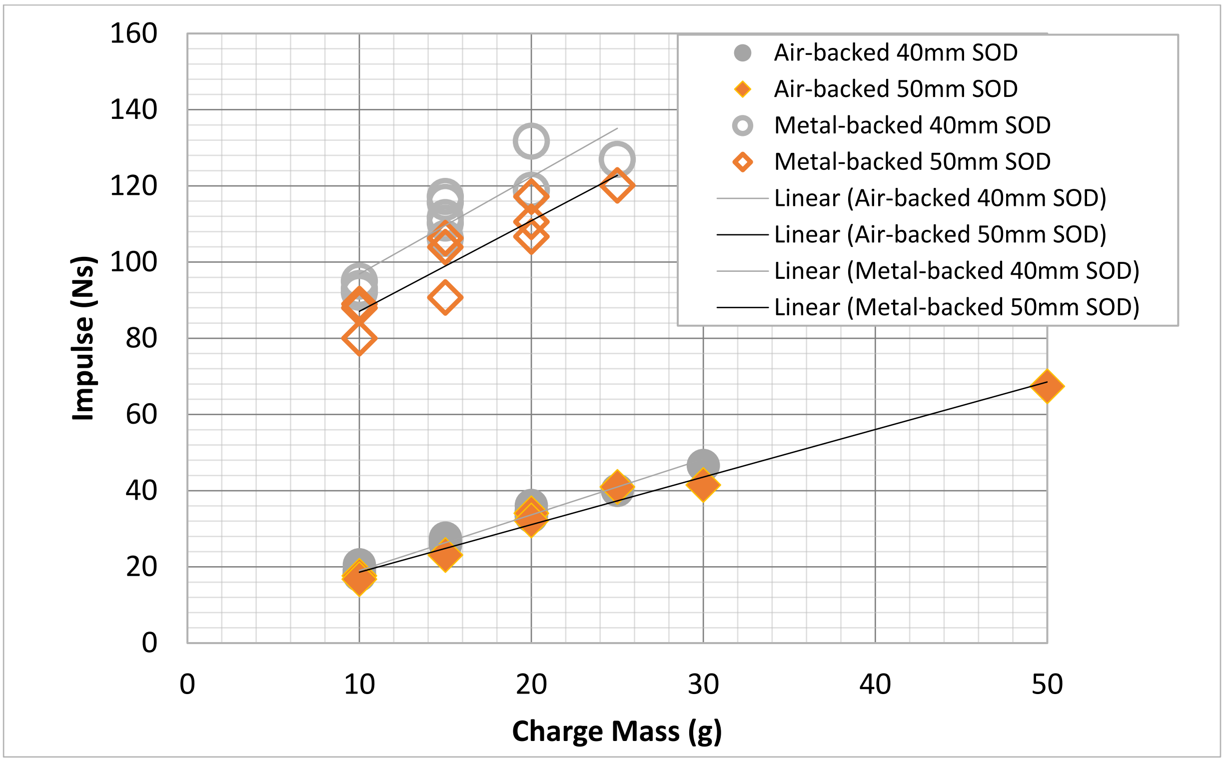

Figure 5: Graph of experimentally measured impulse versus charge mass

The increase in impulsive loading imparted on the plates appears to be significant and varies slightly with an increase in charge mass. This was calculated with reference to the air charges and found to decrease with an increase in charge mass as shown in Figure 6 where the increase is seen to be more than 5 times for 10g charge and 3 times for 25g charges.

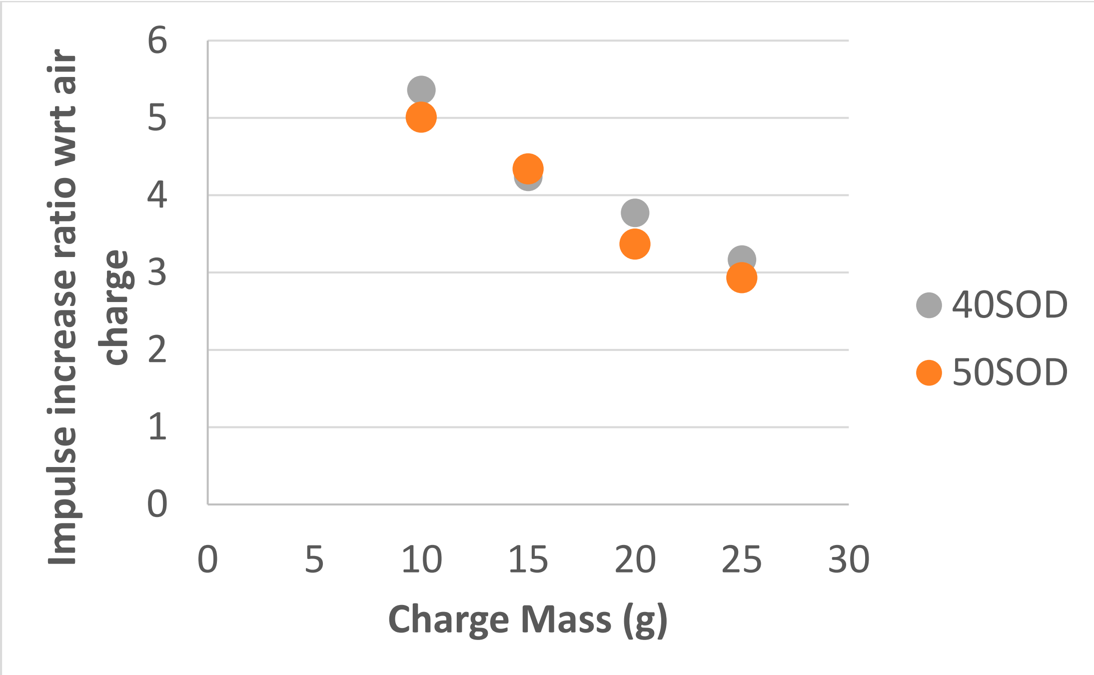

Figure 6 Impulse Increase ratio with respect to air charges for 40mm SOD and 50mm SOD

3.2 Permanent deflections

A summary of the permanent and transient deflections is shown in Table 2 for the metal-backed experiments. The peak transient deflections are larger than the permanent deflections, as expected, with a typical elastic recovery of 2-3 plate thicknesses (slightly larger than expected, except for the 25g metal-backed detonation at a 50 mm SOD). Membrane action and shear stresses would be present as deformation increases in the plate section but without any evidence of rupture due to these internal forces. This was desirable for tests involving high-speed cameras, as torn pieces of the plates could have damaged the camera system, and discontinuities such as cracks would have been difficult to process during digital image correlation.

A graph of final midpoint deflection versus charge mass is shown in Figure 7 for the two types of charge backing. The mid-point deflection increases linearly with increasing charge mass for a given charge backing and SOD combination. The metal backing increased the permanent mid-point deflection of the plates, as might be expected due to the large increase in impulse transfer. However, the difference in deflection is smaller than the rise in impulse, indicating that the relationship between impulse transfer and plate deflection is not straightforward. The physical reason for this is unclear.

Table 2: Average midpoint deflections obtained from the experiments

SOD	Charge Mass	Permanent Midpoint Displacement (mm)		Transient Maximum Midpoint Displacement (mm)	
mm	**(g)**	**air-backed**	**metal-backed**	**air-backed**	**metal-backed**
40	10	14.3	23.2	22.0	31.8
	15	20.9	29.8	25.3	33.4
	20	26.0	34.4	30.3	40.8
	25	31.3	38.4	36.3	42.7
50	10	11.3	21.5	-	28.2
	15	16.1	23.9	21.7	29.8
	20	19.5	28.6	24.7	37.1
	25	25.5	34.4	30.5	36.3
	30	24.2	-	-	-
	50	40.7	-	-	-

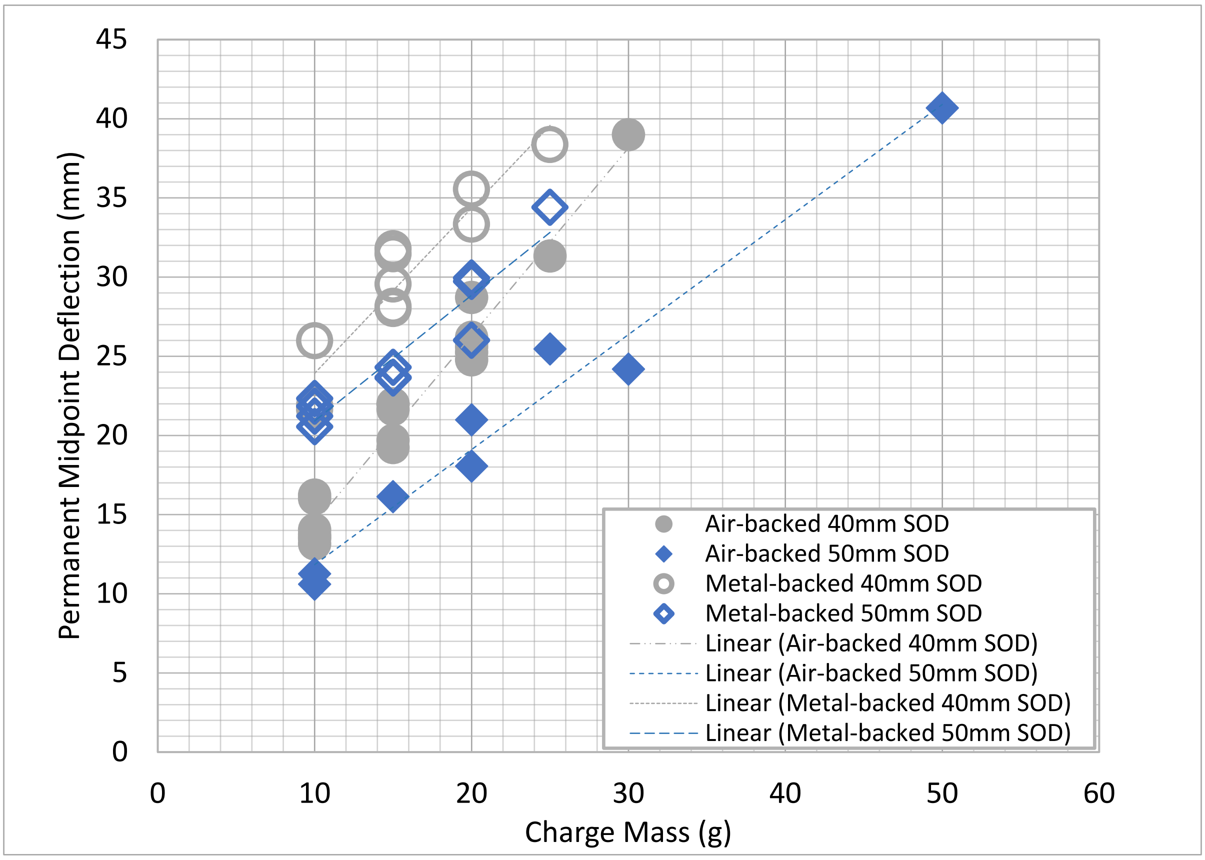

Figure 7: Graph of experimentally measured permanent mid-point deflection versus charge mass

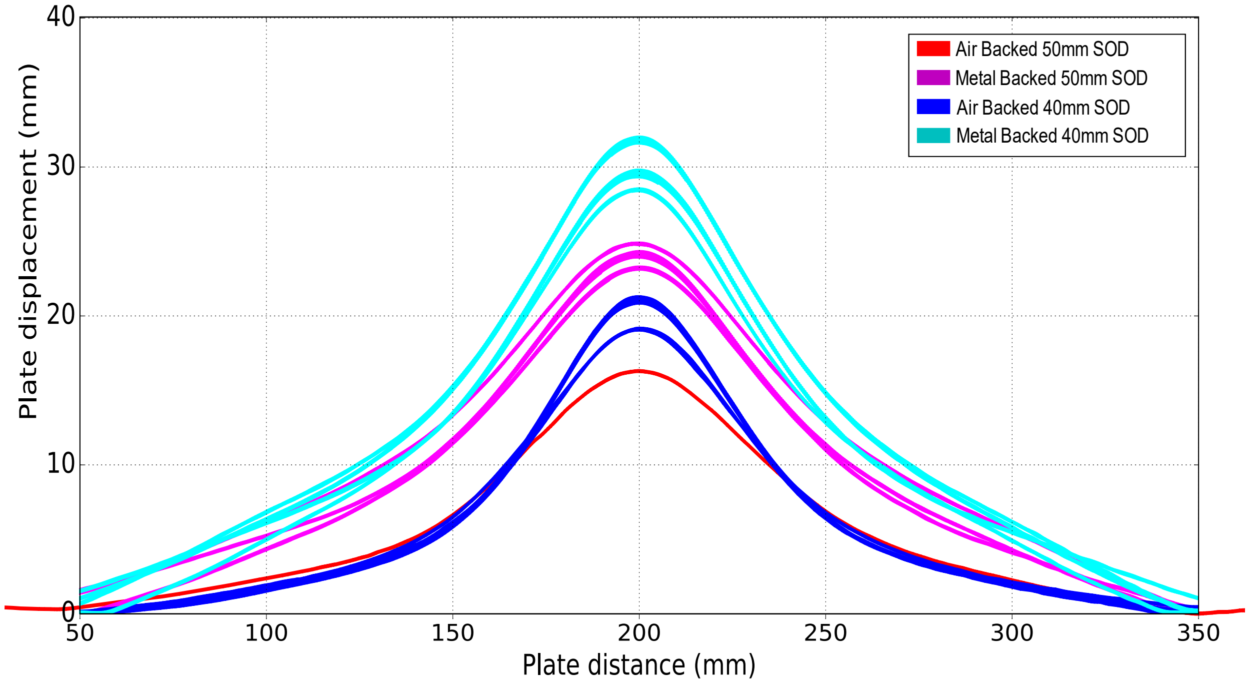

Figure 8: Experimentally measured permanently deformed mid-line profiles from plates subjected to 15g metal-backed detonations

The permanently deformed mid-line plate profiles for the 15g air and metal-backed charge detonation tests are shown in Figure 8. The profiles cluster according to SOD, indicating good repeatability of the loading and response. As expected, the 40 mm SOD plates exhibited higher deflection magnitudes due to load localisation. All the plates exhibited a localized central peak atop a global dome, with the metal-backed test plates appearing to be superficially similar to the air-blast loaded plates. The obvious difference is the mid-point displacement magnitude (which increased with decreasing SOD and with the presence of the metal backing).

The differences in the profile shape become more obvious when the deflections are normalized against peak midpoint deflection, as shown in Figure 9. The air-backed plates exhibited a more localized deformation than the metal-backed plates. For air-backed detonations, the differences in profile shape due to SOD are most evident at 10g, shown in Figure 8a. At 20g and 25g, the air-backed test plate profiles are similar to each other (Figures 8b and 8c), whereas at 10g the profile of the 50 mm SOD air-backed test plates are similar to the 50 mm SOD metal-backed detonations. There is little discernible effect of SOD on profile shape for the metal-backed tests, especially at 20g and 25g. The metal-backed test plate deformation is more localised at 10g but appears more conical at 25g.

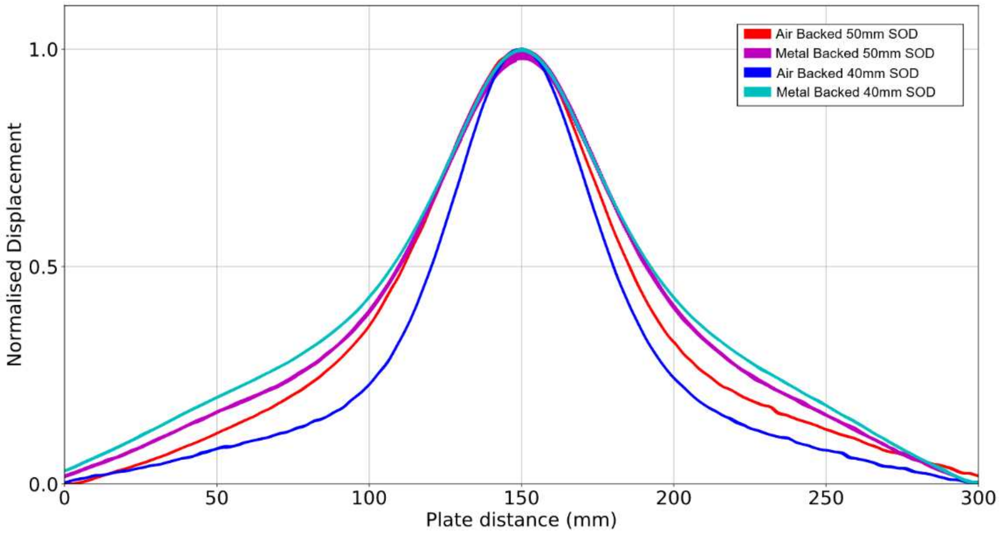

(a) 10g detonation

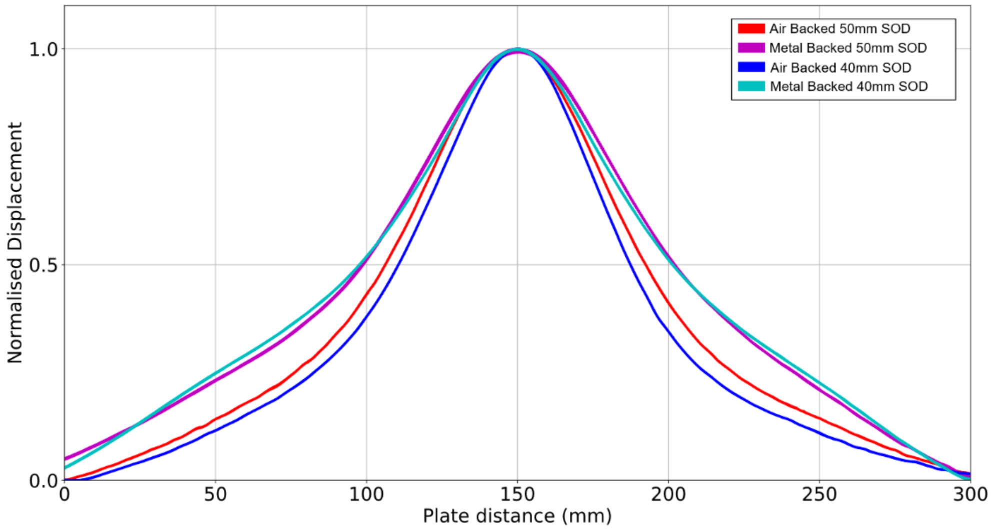

(b) 20g detonation.

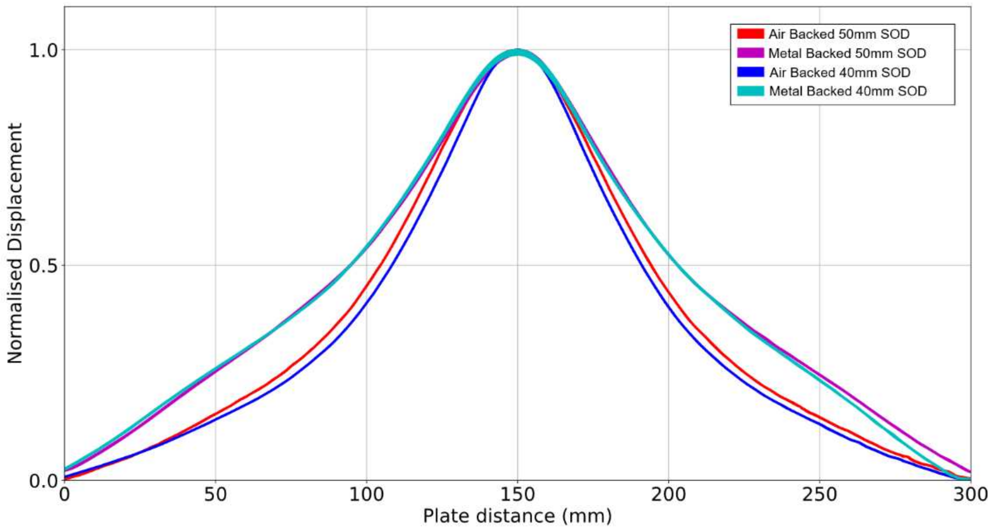

(c) 25g detonations

Figure 9: Normalised out-of-plane permanent displacement profiles for air and metal backed charge detonations

3.3 Transient deflections

The transient data obtained using DIC is presented in two ways. Firstly, the transient deflection-time histories of the midpoint are shown in Figure 10. Secondly, the evolution of the plate profile is illustrated by looking at the out of plane displacement along the mid-line. This is shown at discrete points in time together with the observed final deformation profile in Figures 10-14.

Figure 10a shows mid-point deflection-time histories from 10g metal-backed detonations at different SODs with the red and blue curves representing the experimental results and the black curves representing the simulation results (the simulations are discussed later in the paper). As might be expected, the 50 mm SOD has a consistently lower magnitude transient response in keeping with the permanent deflection observations. The peak mid-point deflections occurred at similar times (approximately 700 μs) in all tests, and the elastic vibration is similar. Figure 10b shows comparable results for 20 g metal-backed detonations. Once again, the 50 mm SOD had a consistently lower magnitude displacement due to the increased SOD. The peak mid-point deflections occurred at the same time and the elastic vibration was similar.

From Figure 10c, which shows mid-point deflection time histories from the 25 g air-backed detonations, it is evident the elastic recovery of the test plates rebounds below the dashed line of permanently deformed plate within the first 2 ms. This did not occur in the metal-backed test plate responses (illustrated in Figure 10a and Figure 10b). The metal-backed rebound characteristic is similar to responses observed in buried charge explosions that have a much longer loading phase due to the ejecta impinging on the test plate (31) (22). The experiments suggest there may be an extended loading duration for the metal-backed detonations that is not present in the air-backed configuration.

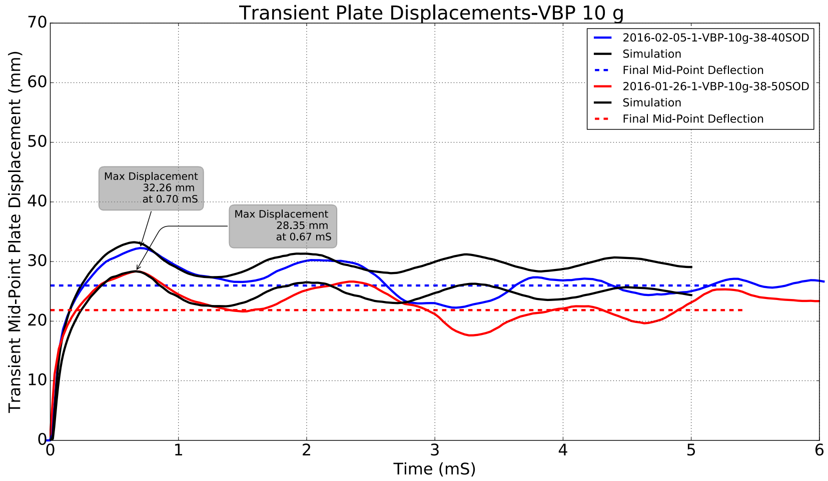

(a)

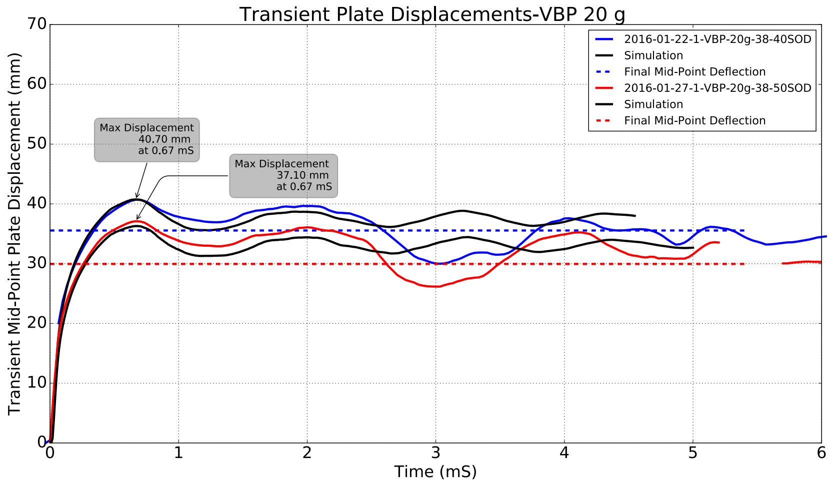

(b)

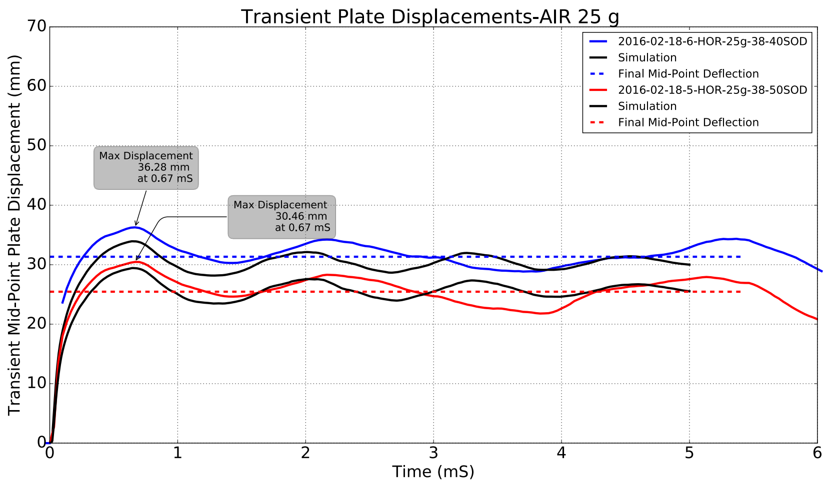

(c)

Figure 10 Transient midpoint deflections obtained using DIC (a) 10 g metal-backed detonations (b) 20 g metal-backed detonations (c) 25 g air-backed detonations, 40 mm SOD

The transient deformation profiles for 10, 15, 20 and 25 g metal-backed detonations are shown in Figure 11 to Figure 14 respectively. On the left hand side of each figure are the air-backed test plates, while the metal back test plate profiles are shown on the right hand side of each figure at the same discrete time intervals. Some of the early time curves at 66 μs (the blue curves) are either slightly irregular or missing due to motion blur, particularly at higher charge masses when the initial velocity of the plate was greater.

The evolution of the profile was similar for each charge mass, but the shape was more localised deformation in the 40 mm SOD series. The metal backed plate deformation first appeared to be localised to a 100mm diameter plastic hinge in the centre of the plate (at 66 μs). The plastic hinge moved radially outward and transitioned into a more global and final profile later in the response. The metal-backed plates exhibited greater deflections, with the difference in the early time response most significant at lower charge masses. Apart from the deflection magnitude, the early-time response was similar in the metal-backed and air-backed test plates, and also similar to findings by Tiwari et al (33) for air-blasted plates.

After 165 μs, the plastic hinge had moved radially outwards and had a 150mm diameter. The shape of the deformed section was conical between the midpoint and the plastic hinge. By 297 μs, the hinge reached a diameter of approximately 250mm and the general profile was bell-shaped with a point of inflection forming at approximately 100mm diameter. Up to this point, the air-back and metal-backed plates followed a similar response, albeit with different peak deflection magnitudes. However, additional deformation along the plate periphery occurred in the metal-backed plates later in the response that was not evident in the air-backed transient deformation profiles.

This point of inflection in the central region became more noticeable and was most pronounced at 561μs as the plate approached its maximum transient deformation (for both air and metal-back test plates). The plates reached maximum transient deformation between 660 and 700 μs, and the point of inflection became less significant. In all cases, it was evident that the transient profile shape varied significantly from the permanently deformed shape measured post-test. This underlines the importance of captured the transient behaviour of blast-loaded structures, even those made from materials with large plastic capacity such as steel, and has implications for the validation of numerical models of blast-loaded steel structures.

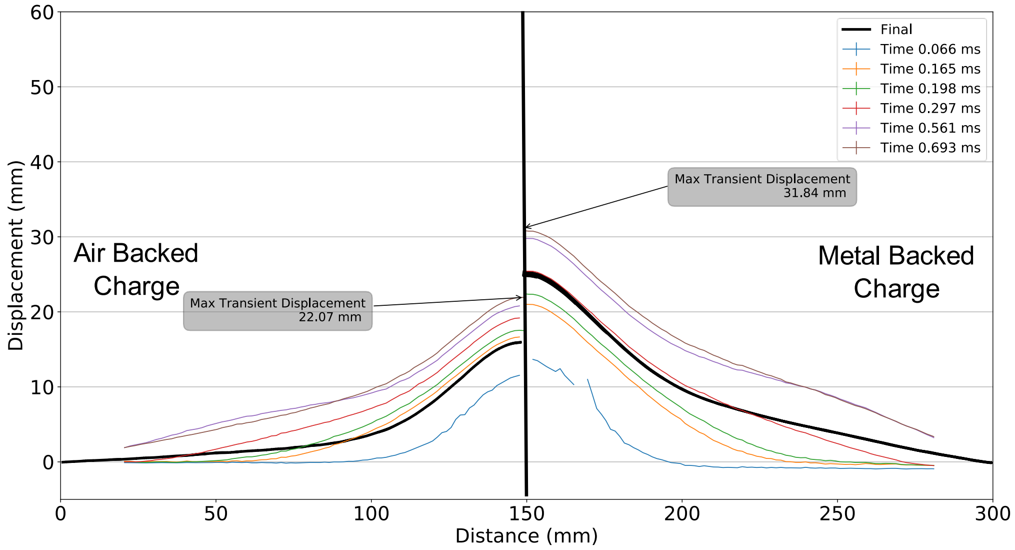

Figure 11: The experimentally measured transient plate profiles for typical 10g detonations (50 mm SOD) for discrete time intervals (colour) and the final deformed plate profile (black).

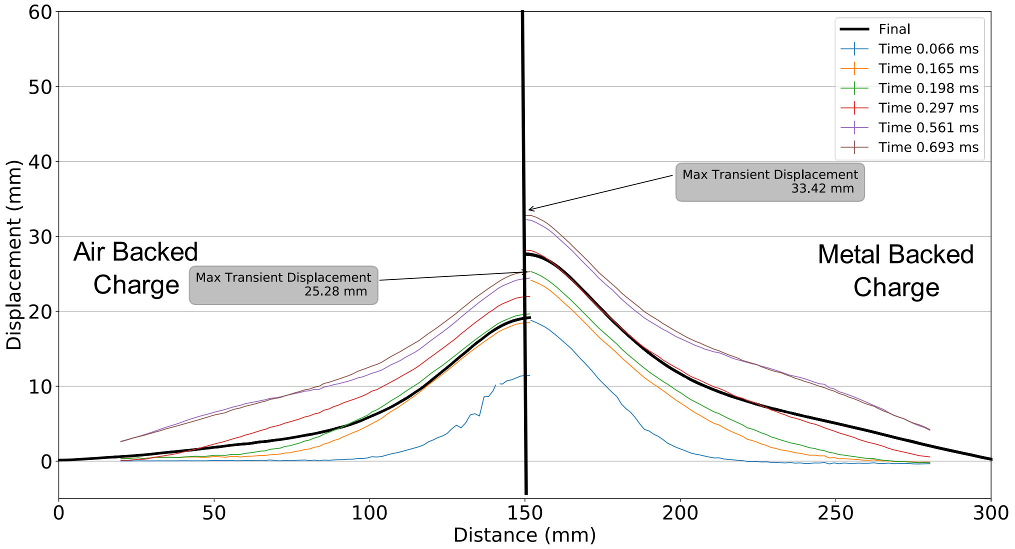

Figure 12: The experimentally measured transient plate profiles for typical 15g detonations (40 mm SOD) for discrete time intervals (colour) and the final deformed plate profile (black).

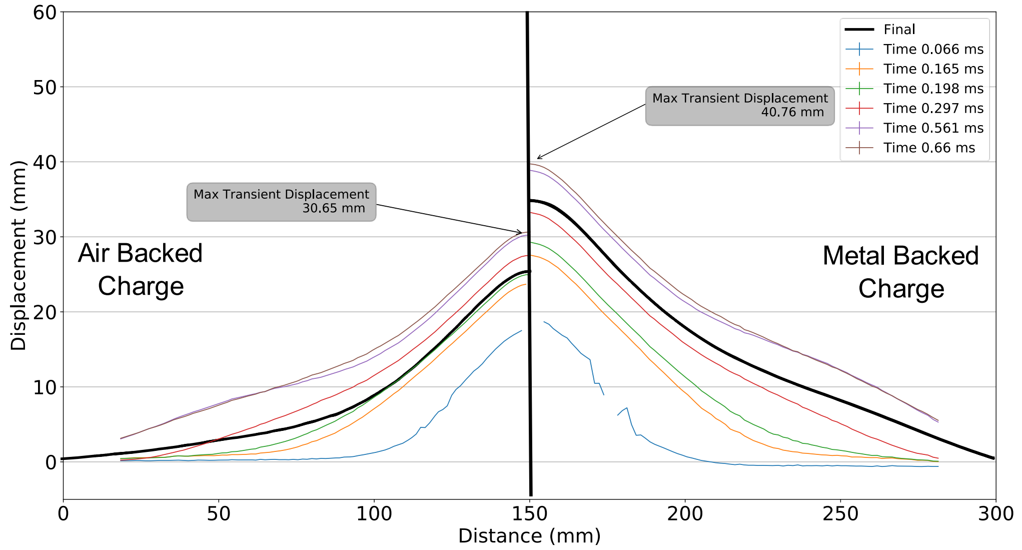

Figure 13: The experimentally measured transient plate profiles for typical 20g (40 mm SOD) detonations for discrete time intervals (colour) and the final deformed plate profile (black).

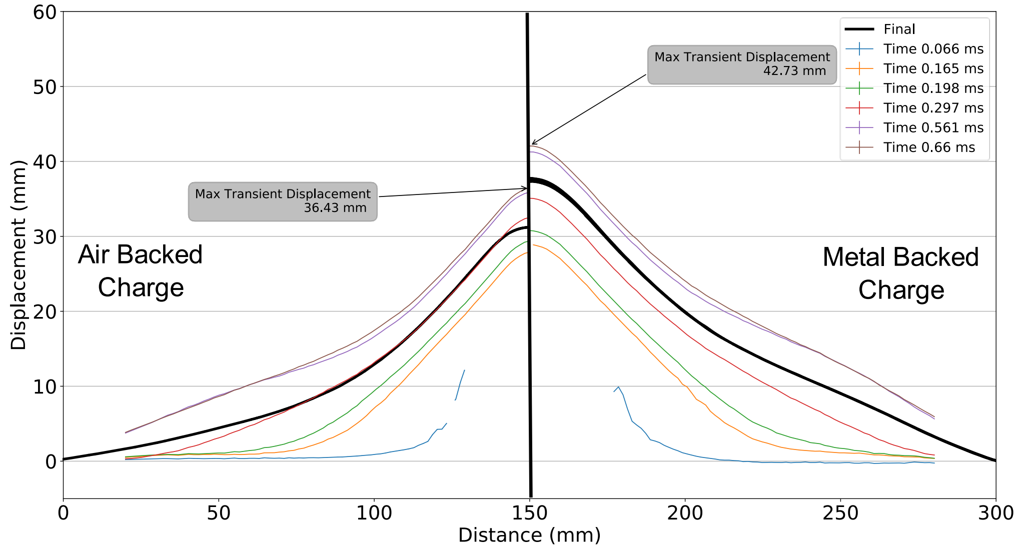

Figure 14: The experimentally measured transient plate profiles for typical 25g detonations (40 mm SOD) for discrete time intervals (colour) and the final deformed plate profile (black).

4. Numerical simulations

A numerical model was developed to aid in the understanding of the transient deformation of the test plate. The test plate, clamp frame and explosive were modelled using the Multi Material Arbitrary Lagrange Eulerian (MMALE) Fluid Structure Interaction (FSI) approach in LS-Dyna. Figure 15 shows a quarter symmetry representation of the models (one for each charge backing type).

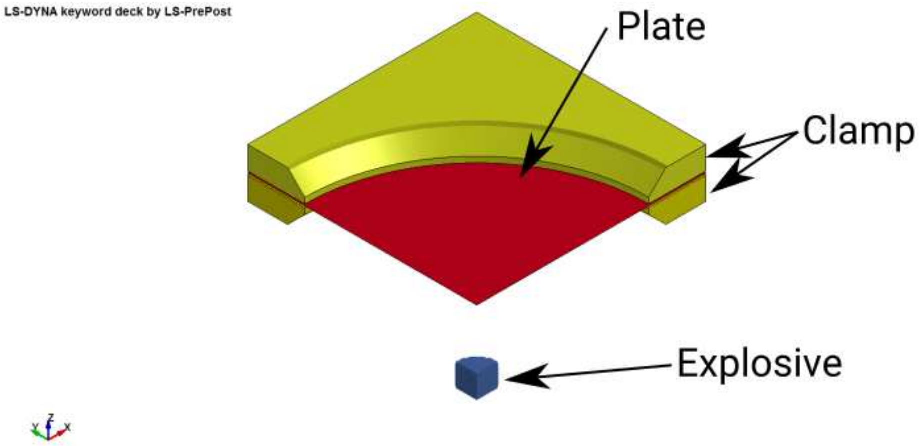

(a) air-backed detonations

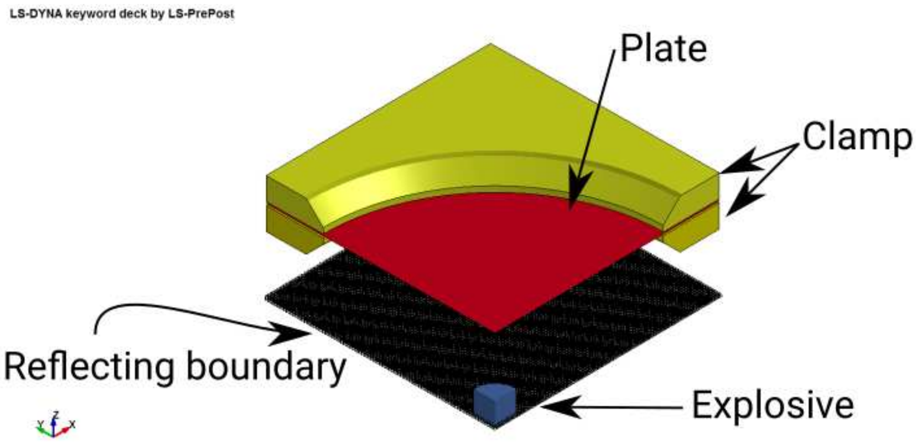

(b) metal-backed detonations

Figure 15: LS Dyna model schematics

4.1 Model components

The test plates were modelled using Lagrangian shell elements (ELFORM 16, fully integrated shell elements) and a Johnson Cook (MAT15) material model which was calibrated using tensile test data which depicted a fracture strain of 35-40% (32). A 2 mm element size was chosen for the test plates as this offered the best compromise between minimising leakage forces and reasonable computational times. Table 3 presents the values used in the material formulations. The maximum plastic strain captured in any of the models was 15% which is well below the 35% noted for fracture of the material and no failure modelling was needed.

Table 3 Material formulation for the test plates. (31)

Material Parameters	Density	Youngs modulus	Poissons Ratio	Taylor Quinney	Specific heat	Reference strain rate
	P	E	V	X	C_p	$\dot{\varepsilon}_0$
	7830 kg/m^3	206 GPa	0.29	0.9	452 KJ	0.0014
Numerical Model Parameters						
Johnson Cook Variable	A	B	n	C	m	
	352 MPa	642 MPa	0.5597	0.032	0.81	

The clamp frames were modelled as an elastic material with a Youngs Modulus of 210 GPa. The bolted connections were modelled using spring elements to simulate the clamping force, which resulted in an equivalent bolted pressure of 240 MPa (similar to results reported by Gerretto (34)). Although this method is not as thorough as modelling the entire bolt and connection, it is effective in producing the clamping force between the two clamp frames that restrain the test plate. this method was considered suitable (and was computationally more efficient than a more complex representation) because no significant pull in or tearing failure was observed during the experiments. A schematic representation of the clamp plate assembly showing the spring elements is given in Figure 16. Contact between the plate and clamp frame was simulated using a surface-to-surface penalty-based contact algorithm with a coefficient of friction of 0.17, based on the findings of Gerretto (34).

The air was represented as a 200x200x200mm block divided into 2mm cubed elements following the results of the mesh convergence study for a similar configuration (34). Geretto (34) found that the size of the air mesh had a much smaller effect than the size of the plate mesh. Two boundary conditions were imposed on this block (to represent the XZ and YZ symmetry conditions) and all other surfaces were defined as free boundaries, allowing out flow of the Eulerian air formulation. The air was modelled using an ideal gas equation of state and a null material. Tracer points were placed at 20 mm intervals from the plate centre (plus an additional point placed 10mm from the plate centre) to predict the pressure at discrete points along the front face of the test plate. These points were selected to line up with the experimental data collected by Rigby et al (24).

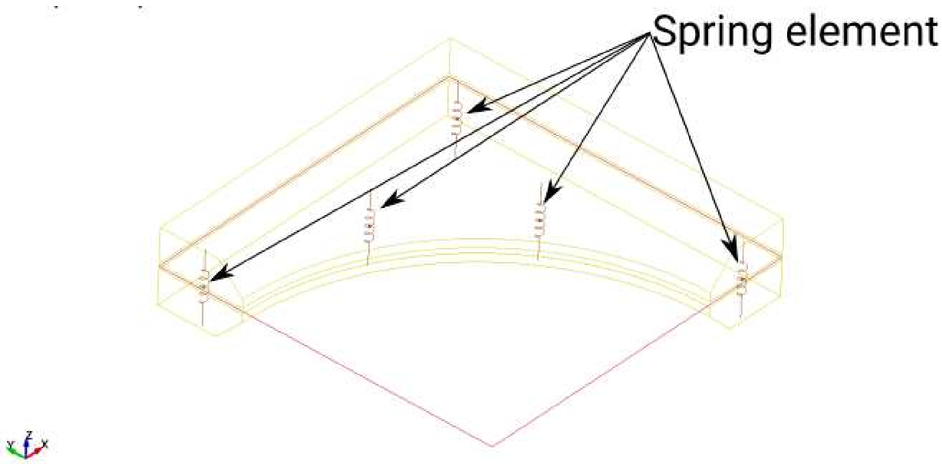

(a) schematic showing the springs used to represent the bolted connections

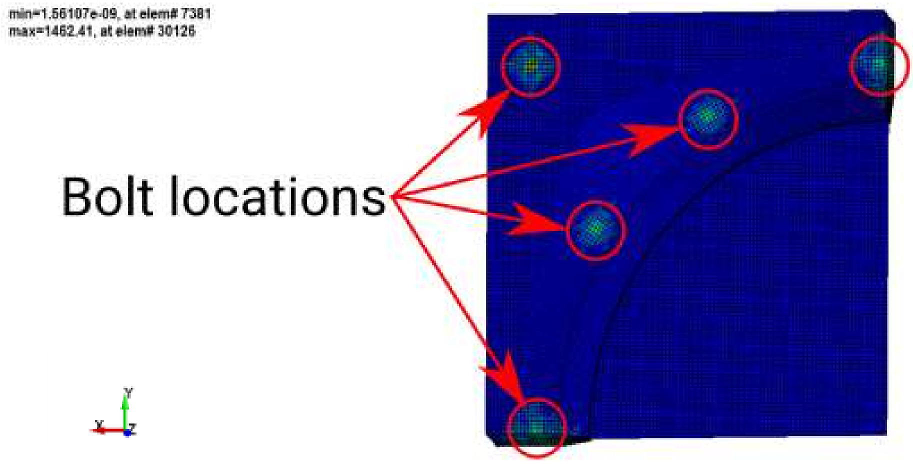

(b) effective stress contour plot showing the clamp bolt points (indicated by the red circles and elevated stress regions) (12)

Figure 16 Representations of the clamp plate assembly

The PE4 was modelled as a cylinder using an initial volume fraction description, which filled the container with the explosive material. The JWL equations of state, in conjunction with the high explosive burn model, were used to describe the explosive shown in Table 4. The volume of the explosive cylinder was discretised into elements that fill the air mesh. The coupling between the explosive products and the test plate was modelled using a penalty-based approach. The metal backing plate was numerically represented as a rigid reflecting boundary condition imposed on the lower node set of the air block when required, by imposing displacement conditions δx, δy and $\delta z = 0$ on the node sets. The ALE fluid flow through the boundary was controlled by implementing ∗ALE_ESSENTIAL_BOUNDARY card that allows for no flow in all directions to be defined on an element set.

Table 4 Table of PE4 properties used

ρ_0 (kg/m^3)	D (m/s)	P_{CJ} (GPa)	A (GPa)	B (GPa)	R_1	R_2	ω	E_0 (GPa)
1616	8193	28	609.77	12.95	4.5	1.4	0.25	9

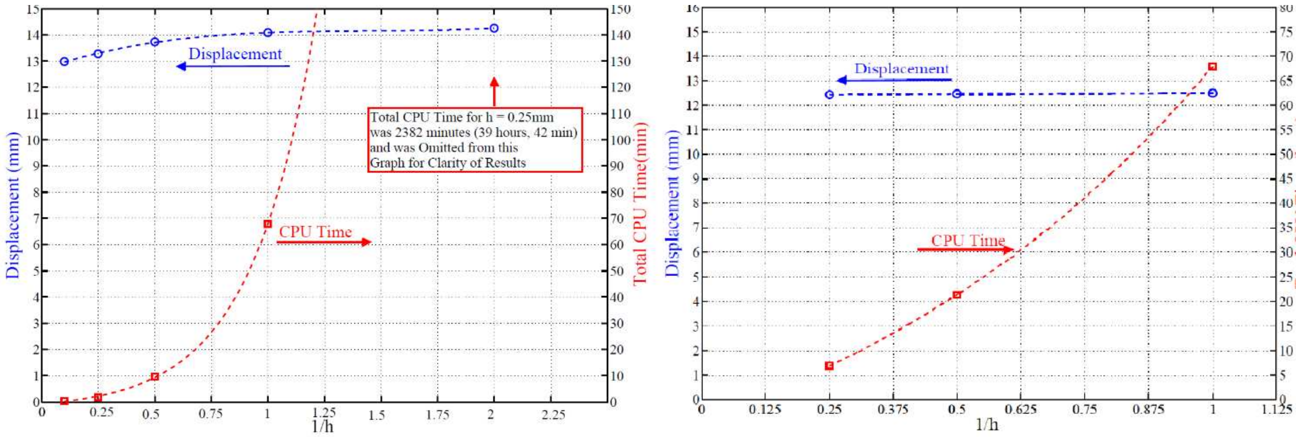

(a) (b)

Figure 17 Mesh sensitivity and convergence analysis for plate mesh (a) and air mesh (b)

A mesh sensitivity and convergence analysis was undertaken as shown in Figure 17, which varied the plate element size (a) and the air mesh size (b). For the plate study a simple spherical charge of 50g PE4 detonated 100mm from the target plate and the pressure was applied using CONWEP. The element length (h) was varied and the computational time required for reasonable convergence was observed. In the plate convergence study, element sizes of smaller than 2mm were found to cause leakage of the explosive products which started to pass through the plate. As a result, the plate mesh size of 2mm was chosen as it optimised the element leakage in the MMALE formulation.

The Air mesh refinement was assessed by varying the element length with the same configuration as the plate mesh, only the MMALE formulation was used. As changes in the air elements had very little effect, a 2mm Air mesh element size was chosen as it was computationally efficient while not effecting the predicted displacement of the plate.

4.2 Running the simulations

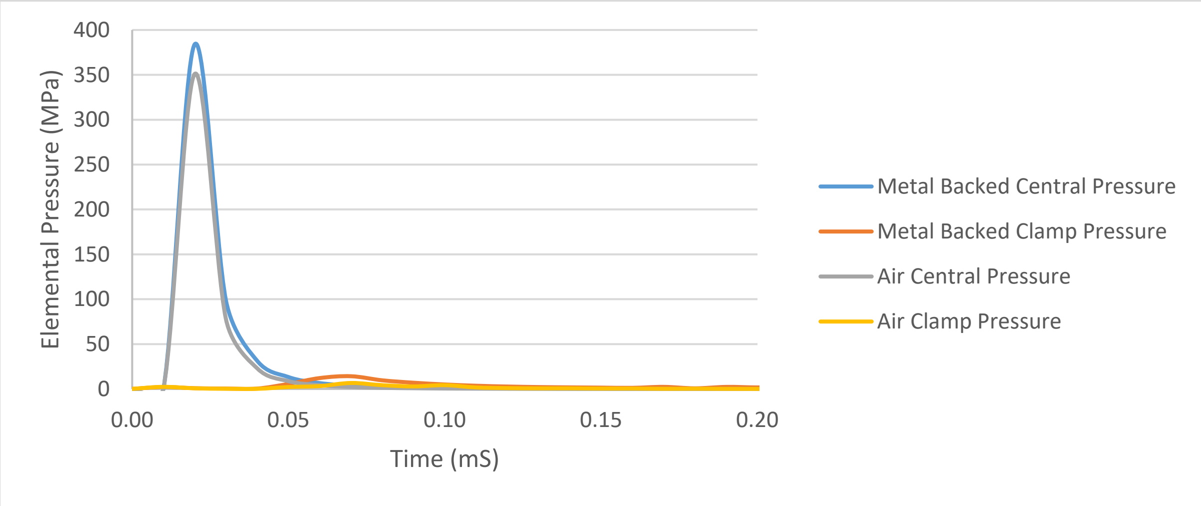

Figure 18 Comparison of the pressure time histories for the two simulations.

The simulations were executed in three phases (loading, deformation, damping). The three phases are illustrated in a typical displacement-time history curve shown in Figure 18. The second and third phases were initiated using a re-start in LS-Dyna that reads the final state of the previous simulation step and modifies the input deck according to the contents of the restart file. During the first phase (loading) the explosive detonated and the explosive products expanded. The resulting pressure wave interacted with the plate, so complete interaction of the MMALE and the test plate was needed. This phase was terminated after 450 µs, which was determined to be sufficient time for the impulse transfer to occur between the Eulerian blast wave, the explosive products and the test plate. Pressure-time histories for the central elements located 1mm before the target plate and the outer elements in the simulations located in the corner of the clamp frame are shown in Figure 20 illustrating that the significant pressure loading event is over inside the first 450 µs that the MMALE was active in the simulation. No significant pressure was measured in the simulations after 450 µs. A 40 MPa peak pressure difference for the two simulations was observed which had the same expected arrival time. The Metal backed simulation shows a slightly longer and higher pressure loading in the centre of the plate and a higher pressure loading at the clamp indicating a higher recirculation pressure.

The Eulerian elements were deleted from the simulation at the beginning of the second (deformation) phase but the Lagrangian elements were allowed to deform. This phase was extended to allow the simulated test plate to plastically deform into its final shape and then elastically oscillate in a similar fashion to that seen in the experimental data. This phase ran from 450 μs to 5000 μs. The final phase applied damping to the plate so that the elastic oscillation of the test plate would settle to its final deformed shape.

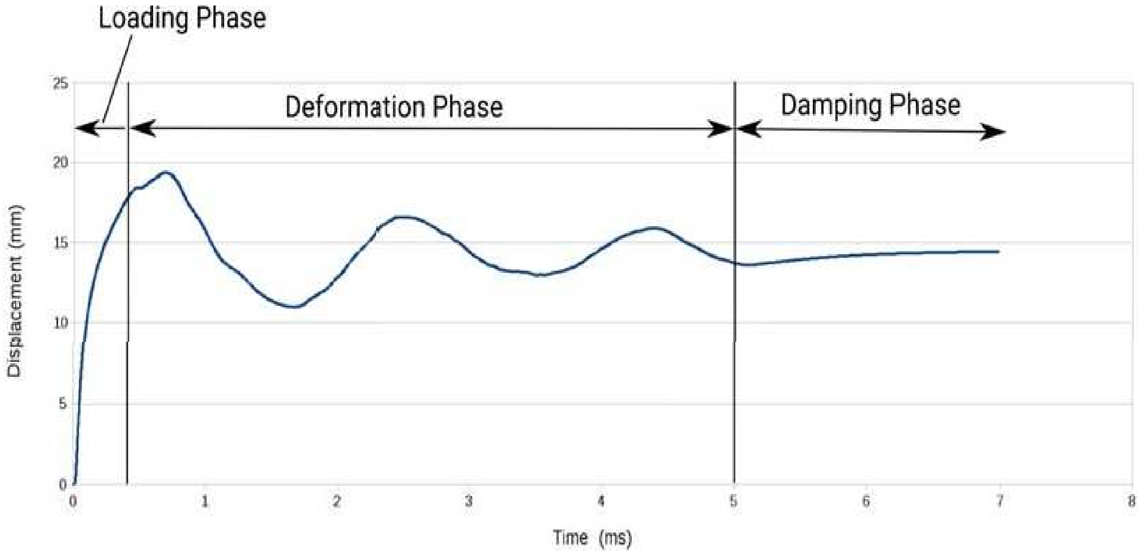

Figure 19: Graph of simulated mid-point deflection versus time, showing the three simulation phases

5. Insights from the numerical simulation results

The simulation results correlate well with the experimental results, as shown in Figure 21, which clearly shows the linear relationship. While there is some scatter in the results, these lie within one plate thickness of variation that is well within the accepted experimental variation expected.

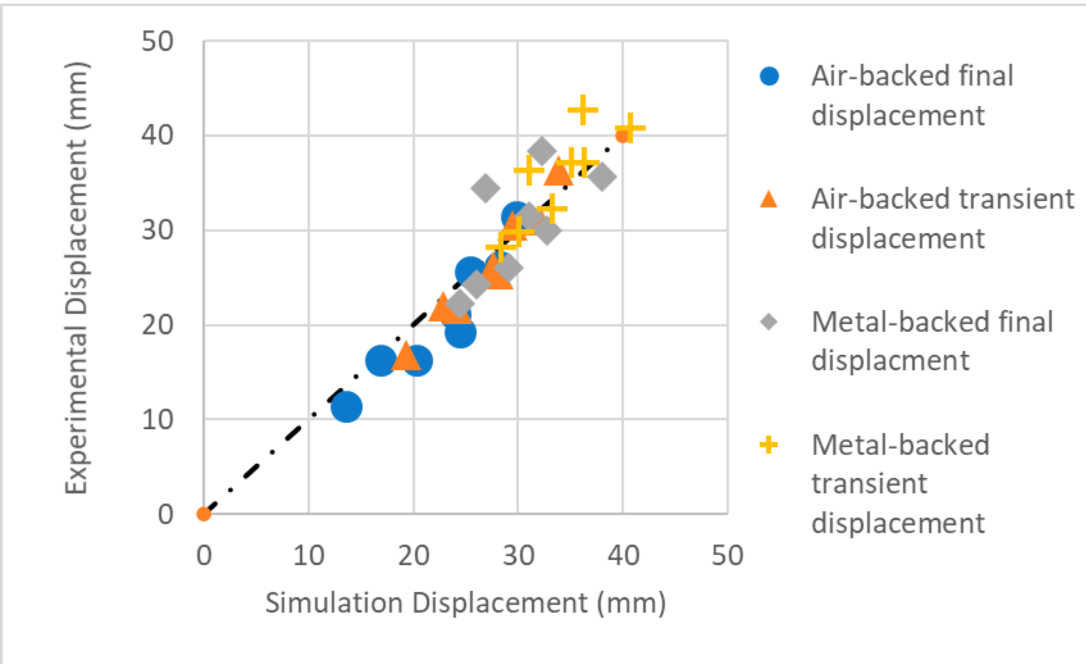

Figure 20: Correlation of experimental and simulation results for both 40mm and 50mm SOD, showing transient and permanent deformation for air-backed and metal-backed charges.

The pressure profiles experienced by the plates are shown in Figure 20. The significant difference in the shape of the initial central loading of the plates can clearly be seen in Figure 20 (a) where the regions in red are pressures higher than 20MPa on the left for the air charge and on the right for the metal backed charge. The high pressure region that interacts with the plate is clearly extending out over a larger central region in the metal backed charge. As this evolves and moves outward toward the clamp boundary the pressures in the air charge drop more than the metal backed charge and the zone located in the clamp boundary is only exposed to pressures of around 10 MPa while the metal backed charge is exposed to over 20 MPa pressures. This clearly shows the re-circulation effect and is one possible place where additional impulse is imparted on the plate without significantly contributing to the plate deformation.

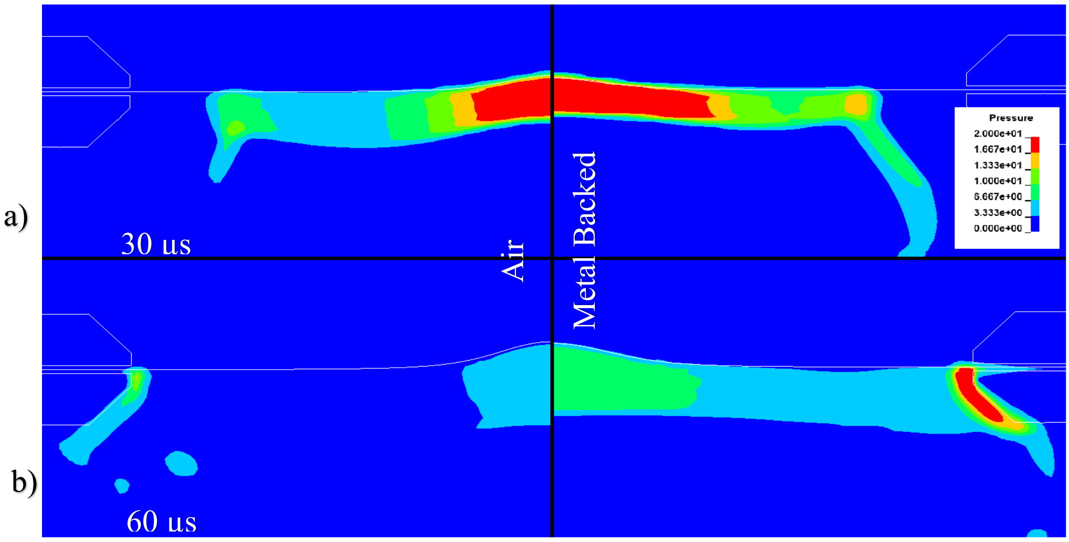

Figure 21 Pressure contours shown at 30 μs (a) and 60 μs (b) for 15g charges of both Air (left) and Metal backed (right) charges.

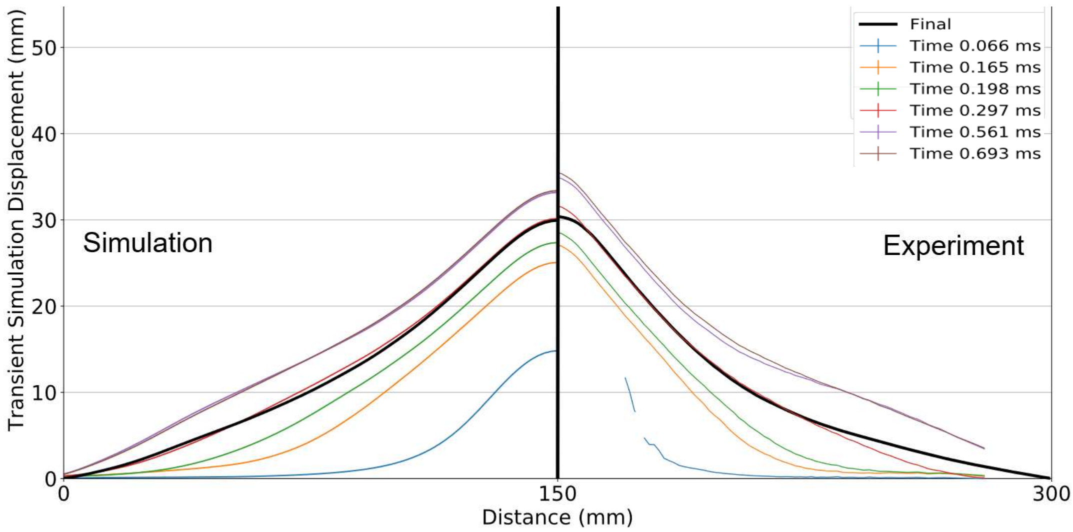

Figure 22: Comparison of simulated and experimental measured transient mid-line displacement profiles for 40 mm SOD, 25g air-backed detonation.

5.1 Air-backed charge simulations

The air backed charge simulations showed that it was possible to approximate the experimental plate deformation results fairly well. The transient mid-point displacement histories were similar to the experiments, illustrated by agreement between the curves shown in Figure 9c for 25g air-backed charge detonations. There is a slightly different period of post-peak oscillation between the simulations and the experiments, with the simulated plate having a slightly shorter period. This was attributed to the slight mismatch between the experimental clamp frame and the more idealised simulated boundary condition.

While the permanent midpoint deflections did not always exactly match the experimental conditions, they were within one plate thickness of the experimental results, considered to be within the limits of experimental repeatability (29) (30). The simulations produced deformed plate profiles that accurately reflected the experimental plate profiles. An example is shown in Figure 22, for a 40mm SOD and 25g PE4 charge. which compares the transient mid-line displacement profiles for the simulations and the experiment. The simulation slightly over-predicts the peak and under-predicts the transient displacement magnitude at the plate centre. The overall evolution of the profile is similar.

5.2 Metal-backed charge simulations

The metal-backed charge simulations closely approximated both the transient midpoint deflections and the final midpoint deflections of the experiments, as evident in Figure 21. The transient mid-point displacement histories were similar to the experiments, illustrated by agreement between the curves shown in Figure 9a and 9b for the 10g and 20g metal-backed charge detonations. The slight elongation in the second peak displacement evident in the experimental at 20g was also present in the simulations, although there is some divergence in the phase of oscillation beyond 3 ms, attributed to the clamp frame idealisation in the simulations.

The transient and final deformed plate profiles for typical simulations of the metal-backed charge configuration are shown in Figure 23. The transient displacement begins in the central region, moving out to the edges, as previously described. As was evident in the air-backed detonation simulations, there is a small over-prediction in the peak and final displacement magnitudes. The very early-time response appears to match the experiment particularly well.

The metal-backed 40mm SOD detonations, across the charge range of 10-25g, have similar normalised permanent plate displacement profiles compared to their experimental counterparts, as shown in Figure 24. The black curves in Figure 24 represent the experimental results while the green curves represent the simulation results. The experimental response is slightly more localised. In general, the curves overlap well, with some small variations in the region of the experimental point of inflection, something that is less visible in the simulations. These figures illustrate how well the simulations captured the overall response of the experiments and lend credibility to the results obtained, particularly the early time impulse and pressure loading.

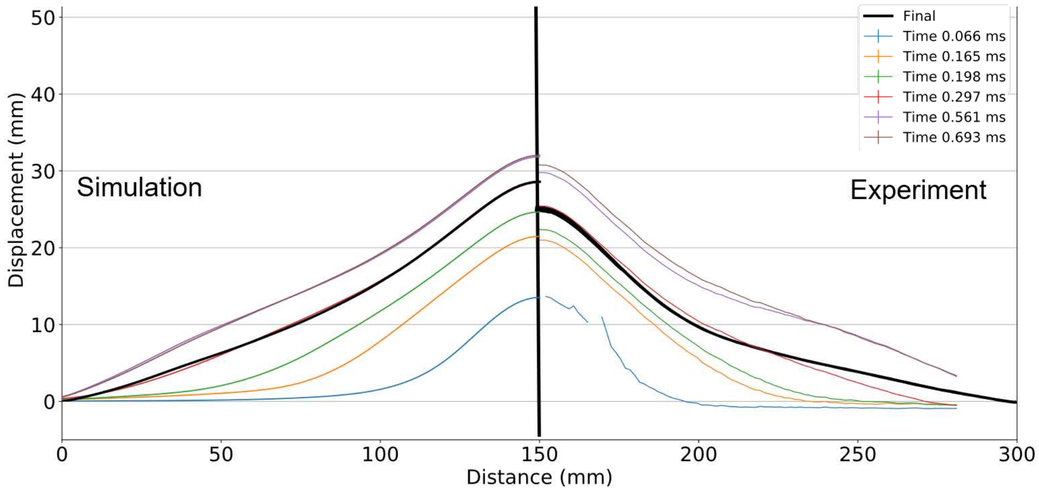

(a) 10 g PE4

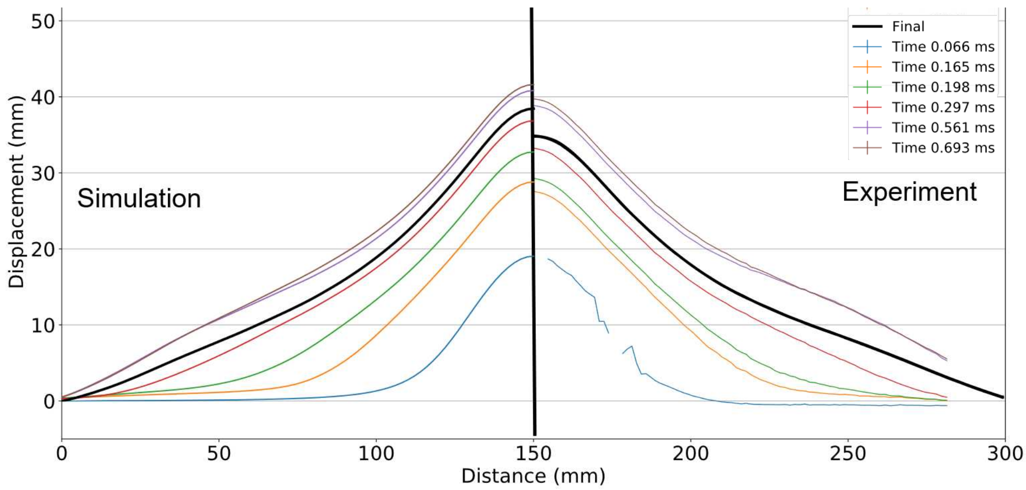

(b) 20g PE4

Figure 23: Comparison of simulated and experimental measured transient mid-line displacement profiles for 40 mm SOD metal backed detonations

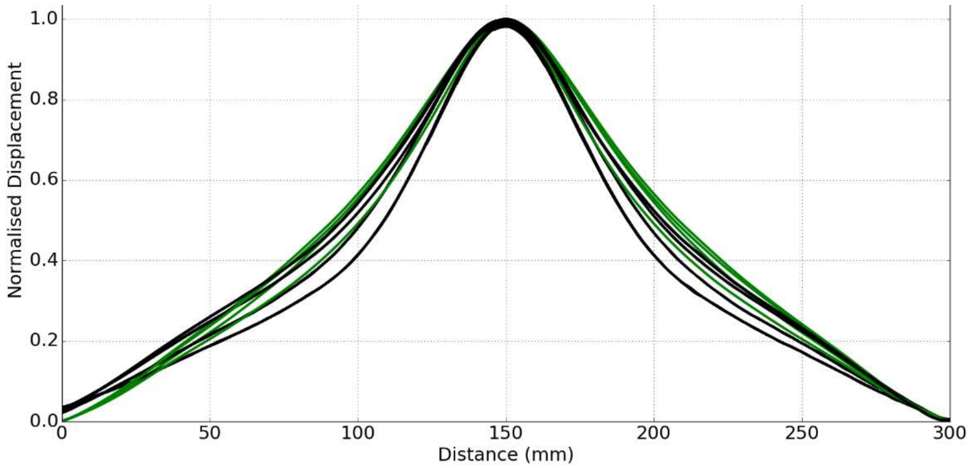

Figure 24 Normalised experimental (black) and simulation (green) final deformed plate profiles for the metal backed configuration at a 40 mm SOD.

5.3 Influence of charge configuration on specific impulse and plate velocity distribution

Figure 25 shows plate velocity and specific impulse predictions for 20 g detonations (D/H = 3.5) for both charge configurations. The simulated pressures indicated that the pressure readings across the whole plate were higher for the metal-backed charge detonations. The specific impulse data, plotted in Figure 25b for a 20g detonation, represents the integral of the pressure-time data across the plate. There is a slight general increase in the impulse across the plate and a more marked increase in impulse along the periphery in the metal-backed detonation simulations. The increase shows that the clamp frame produced a recirculation effect (leading to pressure accumulation) along the clamp boundary (35) that was not present in the air-backed charge detonations. The air-backed charge simulations do not show the pressure accumulation along the boundary, so this is not the result of the clamp frame geometry, unlike the phenomenon noted in reference (36). Nor is it a straightforward charge height effect on the initial forward axial impulse, such as that observed by Kennedy (37).

The metal backing caused reflected pressure from the rigid surface towards the test specimen in the region of the charge. This produced a localised increase in the initial plate velocity, shown in Figure 25a. The localisation effect of the metal backing caused a 40% increase in mid-point plate velocity 30 μs after detonation. The combination of recirculated pressure accumulation at the periphery and the pressure reflection from the detonation on the metal backing surface caused the increased impulse transfer to the plate. The recirculated pressure at the clamp is known to increase the impulse transfer without producing a similar increase in plate deflection (35). This is a reason why the experimentally obtained plate deflections did not increase as significantly as the impulse increased when the metal backing was used.

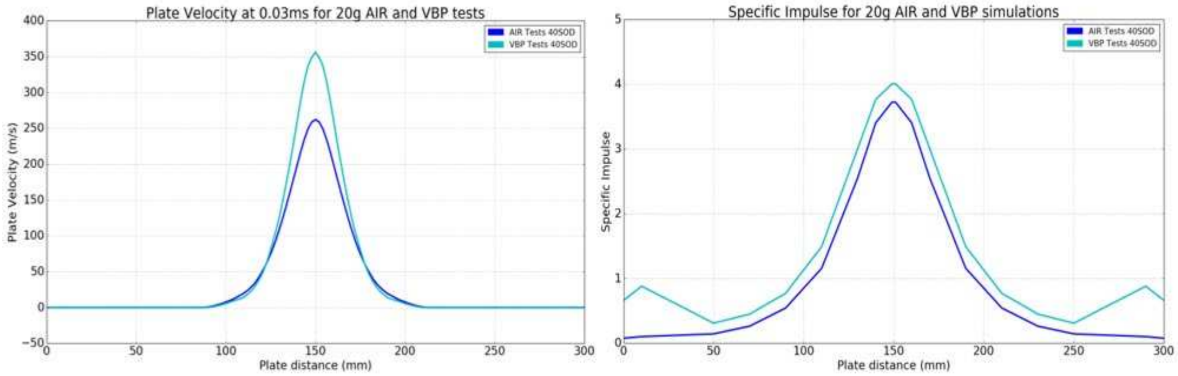

Figure 25: Graphs showing the simulated (a) plate velocity and (b) specific impulse distributions across the plate for the 20g detonations backed by air and metal 40mm SOD

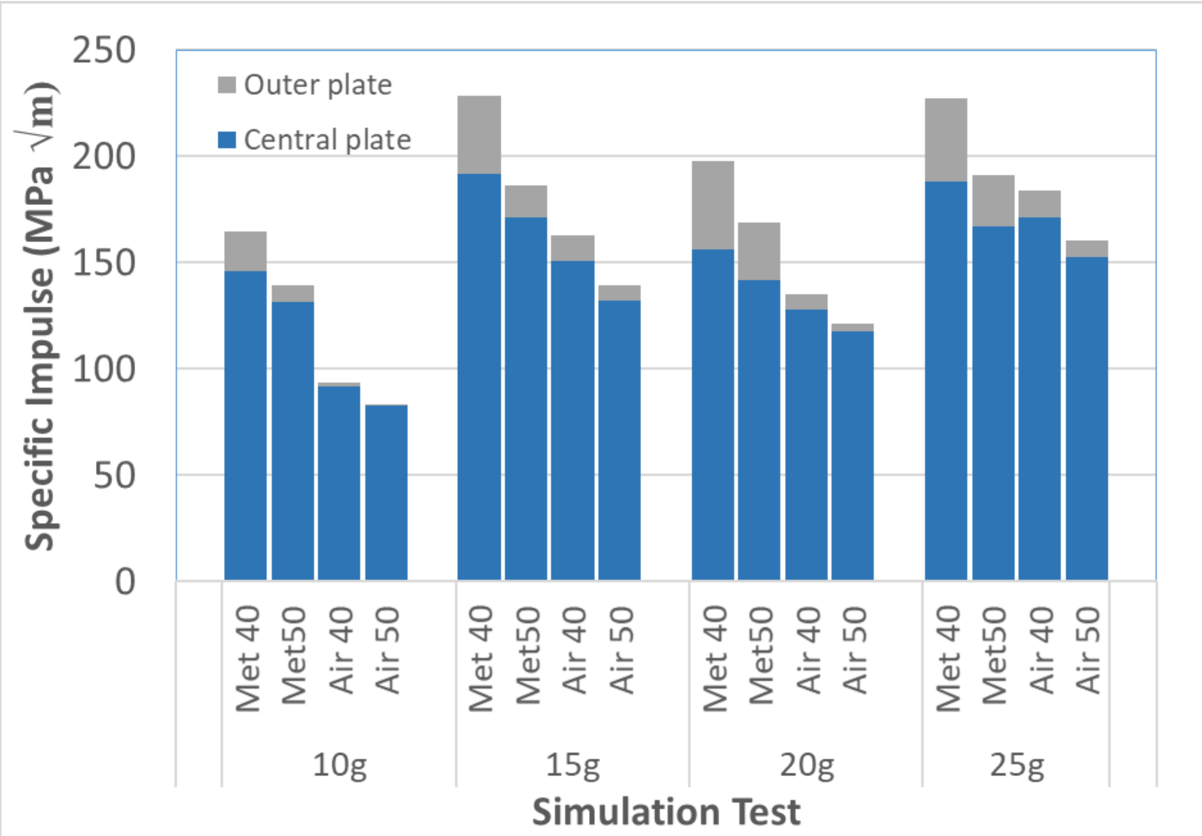

Figure 26: Bar chart showing the simulated specific impulses in the central region and the plate periphery for the air and metal backed detonations (blue indicates the central area, 200 mm diameter, and grey indicated a 50 mm wide outer annulus between the central area and the clamped boundary)

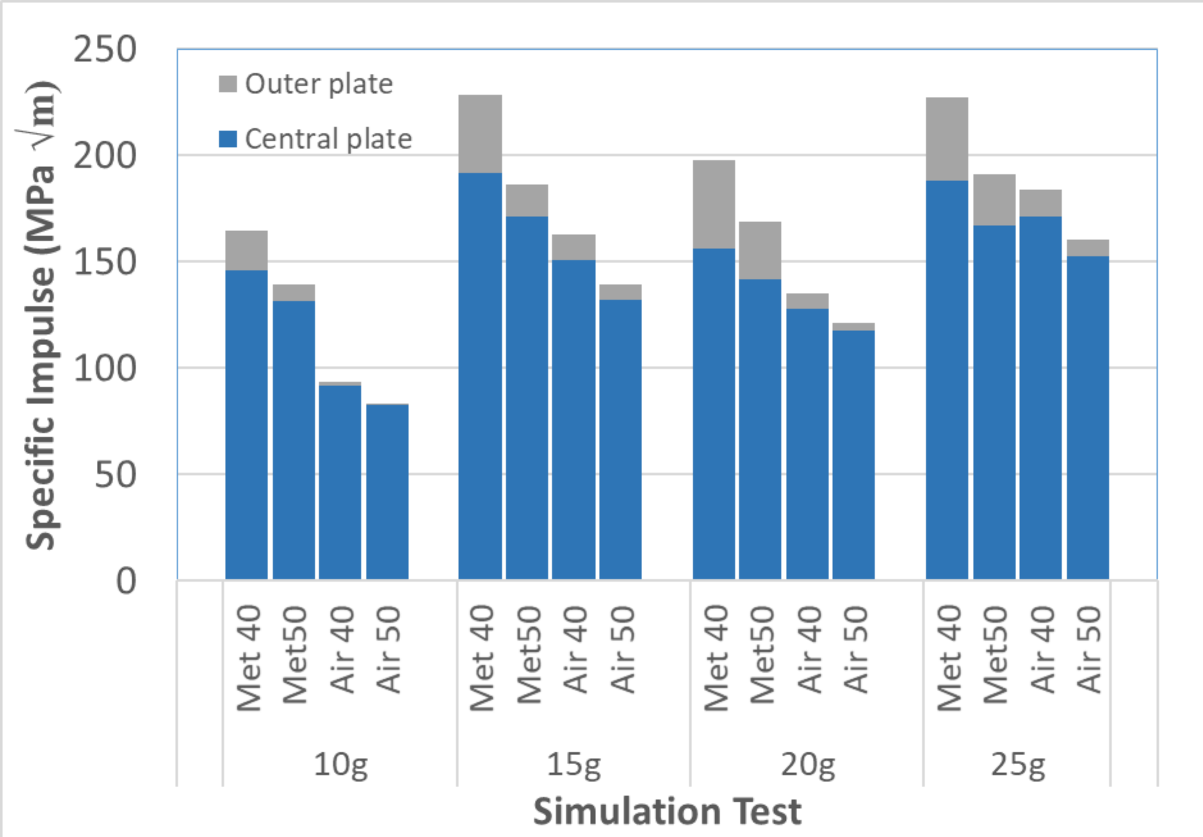

Figure 26 shows a bar chart of the specific impulse distribution in the two plate regions, for different charge masses, SODs and backing types. The blue part is the specific impulse for the central area (200 mm diameter) and the grey part indicates the specific impulse over a 50 mm wide outer annulus (between the central area and the clamped boundary). The results confirm that the observations from Figure 21 (for 20g detonations at 40 mm SOD) apply over the full range of tests reported herein. The central 200 mm diameter portion of the plates experienced an expected increase in impulse with a decrease in SOD. All curves follow the same trend with increasing charge mass, with different magnitudes due to the variation of SOD and charge backing. The influence of charge mass appears non-linear – there was an overall increase in central specific impulse with increasing charge mass, but with a dip in impulse occurring for the 20g charge mass. This decrease at 20g was observed for both the air and metal-backed detonations, and it attributed to charge shape effects at that specific aspect ratio that influence the blast wave propagation towards the plate.

When the specific impulse contribution from the outer 50mm portion of the circular plates was considered, a difference between the metal backed and air backed plates was evident in

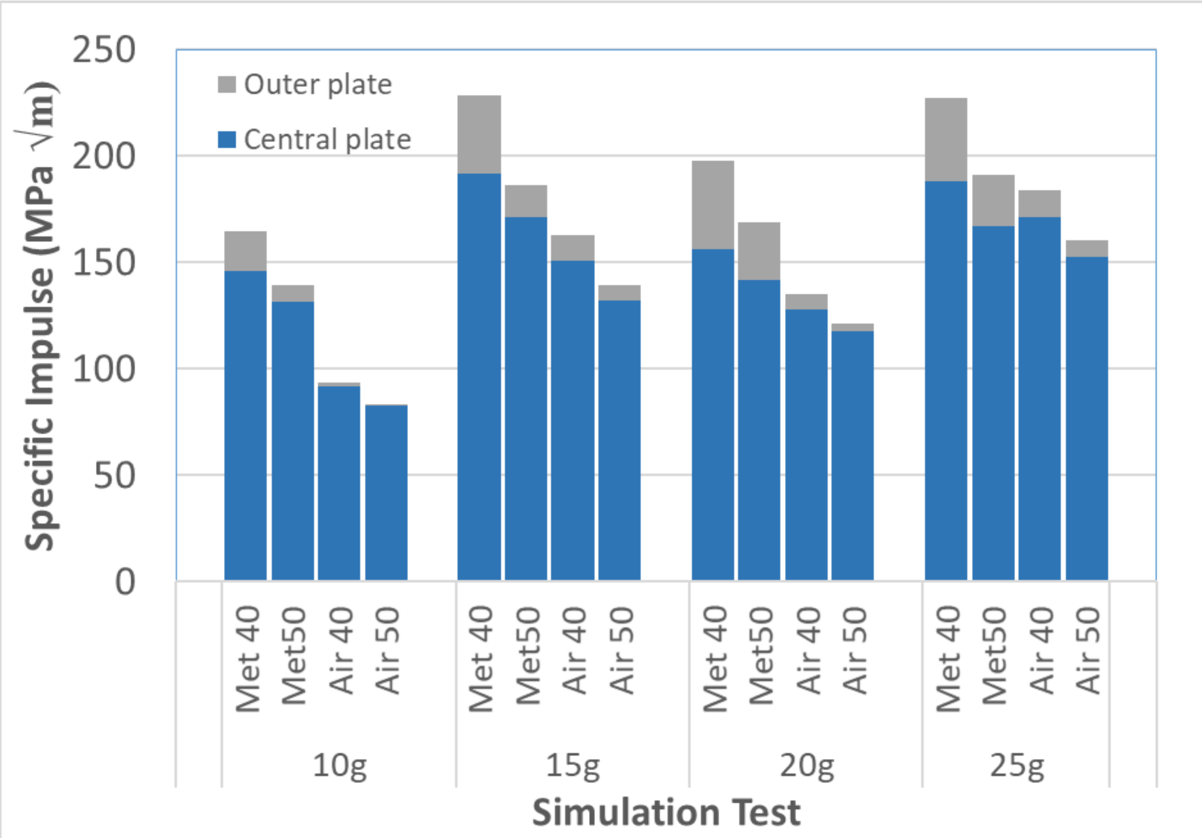

Figure 26. More impulse is imparted to the plates in the outer 50mm portion of the plates when the charge has a metal backing. The air-backed tests show the same dip in specific impulse at the periphery for the 20g detonation. This is not present in the specific peripheral impulse of the metal backed 20g detonations – the opposite trend is observed, with a significant rise in impulse at 20g. The periphery specific impulse was much larger at 40 mm SOD in the metal-backed plate, showing that SOD is a more influential factor when the charge has a solid backing, for the particular test range considered herein. The simulated specific impulse distributions and their sensitivity to SOD and charge backing explain the deformed plate profiles differences evident in the experiments.

6. Conclusions

Experiments and simulations were performed to ascertain the influence of charge backing on the response of plates subjected to blast waves arising from the detonation of plastic explosives. The experiments showed that the impulse imparted to the test plates increased fivefold when the charge was metal-backed. The permanent deflections from the metal-backed detonations were larger than for air, but not to the same degree as the impulse increase.

The simulations revealed two reasons for the increased impulse transfer – pressure recirculation along the clamp not present in the air-backed detonations, and a localised increase in the initial plate velocity in the region of the charge. The localised increase in velocity was due to reflected pressure from the metal back plate towards the test specimen just after detonation. This influenced the deformation of the plate but did not account for the fivefold increase in impulse. The pressure recirculation at the clamp occurred over a larger area and longer duration, causing the impulse to increase without a corresponding rise in plate deflection. The metal-backed detonations were more sensitive to SOD than the air backed detonations, with significantly higher specific impulses at the plate periphery at the 40 mm SOD.

Acknowledgements

The authors are grateful to the UCT University Research Committee, The David and Elaine Potter Foundation and the National Research Foundation (NRF) of South Africa for their financial support. Opinions expressed and conclusions arrived at, are those of the authors and are not necessarily to be attributed to the NRF. The donations of Domex steel from SSAB and Vulcan Steel are gratefully acknowledged. The authors would also like to thank the staff of the Mechanical Engineering workshop at UCT for their assistance in machining the specimens and pendulum parts.

References

1. BBC, (18/07/2018) *China industrial park explosion kills 19.* https://www.bbc.com/news/world-asia-china-44816715

2. Rosenberg, E**.** (17/05/2018), Exploding vape pen caused Florida man's death autopsy says. *Washington Post*, https://www.washingtonpost.com/news/to-your-health/wp/2018/05/16/man-died-after-a-vape-pen-exploded-and-embedded-pieces-into-this-head-autopsy-says/?utm_term=.2e9cfda7d079

3. Peace, Institute for Economics and Global Terrorism Index 2017: measuring and understanding the impact of terrorism. (02/01/2019), http://visionofhumanity.org/app/uploads/2017/11/Global-Terrorism-Index-2017 .pdf

4. GICHD–SIPRI, (03/01/2019) Global mapping and analysis of anti-vehicle mine incidents in 2017, Geneva. *QICHD.* https://www.gichd.org/fileadmin/GICHD-resources/rec-documents/Brochure_AVM_2017_web.pdf

5. Coalition, (03/01/2019) International Campaign to Ban Landmines and the Cluster Munition, The Monitor *Landmine Monitor Report 2018*, www.the-monitor.org/media/2918780/Landmine-Monitor-2018_final.pdf

6. M.M. Ismail, S.G. Murray (1993) *Study of the blast waves from the explosion of nonspherical charges,* Propellants, Explosives, Pyrotechnics, Vol. 18, 132-138.

7. P. Sherkar, J. Shin, A. Whittaker, A. Aref (2016) *Influence of charge shape and point of detonation on blast-resistant design*, Journal of structural engineering, Vol 142(2) , 04015109

8. C.Wu, G. Fattori, A. Whittaker, D.J. Oehlers. (2010) *Investigation of air-blast effects from spherical-and cylindrical-shaped charges.* International journal of protective structures, Vol. 1, 345–362.

9. C.Wu, D.J. Oehlers, M. Rebentrost, J. Leach, A.S. Whittaker. (2009) *Blast testing of ultra-high performance fibre and FRP-retrofitted concrete slabs*, Engineering structures, Vol. 31(9), 2060-2069.

10. Tyas, A. (2018) *Experimental measurement of pressure loading from near-field blast Events: techniques, findings and future challenges*. Proc 18th Int Conf Exper Mech. Vol. 2(8), page 471.

11. W. Xiao, M. Andrae, N. Gebbeken.*(2020) Effect of charge shape and initiation configuration of explosive cylinders detonating in free air on blast-resistant design*, Journal of structural engineering, Vol. 146 (8), 04020146.

12. R. Qi, G.S. Langdon, T.J. Cloete, S. Chung Kim Yuen. *(2020) Behaviour of a blast-driven ball bearing embedded on a rear detonated cylindrical explosive,* Submitted to IJIE.

13. G.H. Guerke, G. Scheklinski-Glueck. *(1982) Blast parameters from cylindrical charges detonated on the surface of the ground,* Fraunhofer-Inst Fuer Kurzzeitdynamik-Ernst-Mach-Inst Freiburg Im Breisgau (Germany Fr).

14. Tancreto, J.E**.** (1975) *Report No. CEL-TN-1390: Effects of charge shape and composition on blast environment.* Civil Engng Laboratory (Navy).

15. W. Xiao, M. Andrae, N. Gebbeken. (2020) *Influence of charge shape and point of detonation of high explosive cylinders detonated on ground surface on blast-resistant design.*, International journal of mechanical science, Vol. 181, 105697.

16. D. Bergeron, R. Walker, and C. Coffey. (1998) *Detonation of 100-gram anti-personnel mine surrogate charges in sand a test case for computer code validation,* Defence Research Establishment Suffield.

17. D.M. Bergeron, J.E. Trembley. (2000) *Canadian research to characterize mine blast output.* Proc. 16th Int. Symp. on the Military Aspects of Blast and Shock, Oxford, UK. 501–511.

18. C.E. Anderson, T. Behner, and C.E. Weiss *(2011) Mine blast loading experiments,* International Journal of Impact Engineering, Vol. 38(8-9), 697–706.

19. S.D. Clarke, J. Warren, A. Tyas. (2011) *The influence of soil density and moisture content on the impulse from shallow buried explosive charges.* Proc. 14th Int. Symp. Interaction Effects of Munitions with Structures (ISIEMS14).

20. S.D. Clarke, S.D. Fay, J.A. Warren, A. Tyas, S.E. Rigby, J.J. Reay, R. Livesey, I. Elgy. (2017) *Predicting the role of geotechnical parameters on the output from shallow buried explosives.* International Journal of Impact Engineering, Vol 102, 117-128.

21. S.D. Clarke, S.E. Rigby, S.D. Fay, A Barr, A. Tyas, M. Gant, I. Elgy (2020) C*haracterisation of buried blast loading.* Proc. Royal Soc. A: Mathematical, Physical & Engng Sci, Vol. 476(2236), 20190791.

22. E.G. Pickering, S. Chung Kim Yuen, G.N. Nurick, and P. Haw. (2012) *The response of quadrangular plates to buried charges*, International Journal of Impact Engineering, Vol 49, 103–114.

23. A. Neuberger, S. Peles, D. Rittel. (2007) *Scaling the response of circular plates subjected to large and close-range spherical explosions. Part II: Buried charges.*, International Journal of Impact Engineering, Vol. 34(5), 987-882.

24. S.E. Rigby, S.D. Fay, S.D. Clarke, A. Tyas, J.J. Reay, J.A. Warren, M. Gant, and I. Elgy. (2016) *Measuring spatial pressure distribution from explosives buried in dry Leighton Buzzard sand*, International Journal of Impact Engineering, (96), 89–104.

25. NATO. (2014) Procedures for evaluating the protection level of logistic and light armoured vehicles volume 2 for mine threat. Technical Report AEP-55 vol 2. *NATO Standardization Agency*.

26. Voisin A., Pariente J. , Lemercier S. , Soulat D. , Boussu F (2019). *Different Composite Behaviours under Blast Loading.* Switzerland : Trans Tech Publications Ltd, ISSN: 1662-9795, Vol 812, 84-91.

27. Jones, N. (1989) *Structural Impact,* Cambridge University Press.

28. Martin, G.N. Nurick and J.B. (1989) *Deformation of thin plates subjected to impulsive loading - a review. part 1: Theoretical considerations*, International Journal of Impact Engineering, Vol 8, 159–169.

29. Martin, G.N. Nurick and J.B. (1989) *Deformation of thin plates subjected to impulsive loading - a review. part 2: Experimental studies.*, International Journal of Impact Engineering, Vol 8, 171-186.

30. S. Chung Kim Yuen, G. N. Nurick, G. S. Langdon, Y. Iyer. (2017) *Deformation of Thin Plates Subjected to Impulsive Load: Part III – An update 25 years on.*, International Journal of Impact Engineering, Vol 107, 108-117.

31. R.J. Curry and G.S. Langdon (2017) *Transient response of steel plates subjected to close proximity explosive detonations in air*, International Journal of Impact Engineering, Vol 102, 102–116.

32. Curry, R.J. (2017) *Response of plates subjected to air-blast and buried explosions, PhD Thesis*, University of Cape Town.

33. V. Tiwari, M.A. Sutton, S.R. McNeill, S. Xu, X. Deng, W.L. Fourney, and D. Bretall. (2009) *Application of 3d image correlation for full-field transient plate deformation measurements during blast loading.*, International Journal of Impact Engineering, Vol 36(6) 862 – 874.

34. Geretto, C. *(2012) The Effects of Different Degrees of Confinement on the deformation of Square Plates Subjected to Blast Loading, PhD thesis,* University of Cape Town.

35. Nurick, D. Bonorchis and G.N. (2007) *The effect of welded boundaries on the response of rectangular hot-rolled mild steel plates subjected to localised blast loading*, International Journal of Impact Engineering, Vol 34, 1729–1738.

36. Nurick, D. Bonorchis and G. N. (2009) *The influence of boundary conditions on the loading of rectangular plates subjected to localised blast loading – Importance in numerical simulations.*, International Journal of Impact Engineering, Vol 36(1), 40–52.

37. Kennedy, J.E*(1972) Explosive output for driving metal,* Proceedings of the 12th Annual Symposium of the New Mexico Section of the ASME.